UNIVERSITY OF SOUTHAMPTON

Resonant Energy Transfer in Light Harvesting and Light Emitting Applications

by

Soontorn Chanyawadee

A thesis submitted in partial fulfillment for the degree of Doctor of Philosophy

in the

Faculty of Engineering, Science and Mathematics

School of Physics and Astronomy

November 2009

Declaration of Authorship

I, Soontorn Chanyawadee, declare that this thesis titled, 'Resonant Energy Transfer in Light Harvesting and Light Emitting Applications' and the work presented in it are my own. I confirm that:

- This work was done wholly or mainly while in candidature for a research degree at this University.
- Where any part of this thesis has previously been submitted for a degree or any other qualification at this University or any other institution, this has been clearly stated.
- Where I have consulted the published work of others, this is always clearly attributed.
- Where I have quoted from the work of others, the source is always given. With the exception of such quotations, this thesis is entirely my own work.
- I have acknowledged all main sources of help.
- Where the thesis is based on work done by myself jointly with others, I have made clear exactly what was done by others and what I have contributed myself.

Signed:

Date:

UNIVERSITY OF SOUTHAMPTON

Abstract

Faculty of Engineering, Science and Mathematics

School of Physics and Astronomy

Doctor of Philosophy

by Soontorn Chanyawadee

The performance of light emitting and light harvesting devices is improved by utilising resonant energy transfer. In lighting applications, the emission energy of a semiconductor heterostructure and the absorption of organic dyes or colloidal quantum dots (QDs) are engineered so that the excitations in the semiconductor heterostructure can be transferred to the light emitters by means of resonant energy transfer. The emitters subsequently emit colour-tunable light ranging from the visible to the near-infrared. As a result, a twofold enhancement of QD emission is demonstrated in a hybrid QD/semiconductor heterostructure. In light harvesting applications, a hybrid structure of colloidal QDs and a quantum well (QW) *p-i-n* heterostructure is investigated. After highly absorbing QDs absorb photons, the excitations are efficiently transferred to a QW *p-i-n* heterostructure via resonant energy transfer. The generated electron-hole pairs in the heterostructure are subsequently separated by the built-in electric field and collected by the corresponding electrodes. In order to increase the energy transfer rate, the donor-acceptor separation distance is minimised by fabricating channel structures on the heterostructure surface penetrating its active layers. Consequently, a sixfold enhancement of photocurrent conversion efficiency is demonstrated. Photocurrent of the hybrid structure is further improved by replacing the QW heterostructure with a bulk *p-i-n* heterostructure which has higher carrier transport efficiency. Hence, the photocurrent of the hybrid bulk heterostructure is about two orders of magnitude higher than that of the hybrid QW heterostructure. The proposed hybrid structures offer efficient light harvesting devices where high absorption of the colloidal QDs is utilised and their low charge transfer is overcome.

Acknowledgements

Many people have contributed to this thesis and I am very grateful for their support and encouragement.

I would like to thank my supervisor, Prof Pavlos Lagoudakis, for his supervision and encouragement during my PhD. It was him who gave me a great opportunity to come to England and have this unforgettable experience. I should mention Prof Richard Harley, who gives me valuable advice. Many thanks go to my friends and colleagues, specifically Stefan Rohrmoser and Peter Eldridge, who always give me support.

It is my great pleasure to thank my sponsor, The Royal Thai Government, for financial support.

I would like to thank my family who always support me. Without their support, it is impossible for me to do this alone. Thank you very much.

Contents

List of Figures

List of Tables

This thesis is dedicated to my family

Chapter 1

Introduction

Resonant energy transfer (RET) [1, 2] is an interaction between donors and acceptors where excitation energy of the donors can be nonradiatively transferred to the acceptors. Resonant energy transfer was first experimentally observed by Cario and Franck in 1923 [3]. First experimentally studied in molecular systems, resonant energy transfer has been investigated in various material systems such as hybrid structures of semiconductor quantum wells (QWs) and colloidal quantum dots (QDs) [4, 5, 6], hybrid structures of semiconductor QWs and organic materials [7, 8], layer-by-layer polymer films [9, 10] and colloidal QDs [11, 12]. There are many applications of resonant energy transfer including light emitting diodes (LEDs) [13, 14], organic light emitting diodes (OLEDs) [15, 16, 17], lasers [18, 19], biosensors [20, 21], light harvesting devices [22, 23] etc.

In order to address the impending shortage of energy resources, the studies here will focus on improving the performance of light emitting and light harvesting devices by utilising resonant energy transfer. Since light emitting devices consume

almost 20% of worldwide energy usage, a considerable amount of energy can be saved if the efficiency of these devices is improved. There have been many efforts to produce highly efficient light emitting devices during the last decades. Owing to mature technology of semiconductor fabrication, solid state light emitting devices with high internal quantum efficiency can be produced [24]. However, these light emitting devices suffer from total internal reflection at the device/air interface due to high refractive index (n) of the device materials compared to the refractive index of air (n_{GaN}=2.3, n_{GaAs}=3.3, n_{air}=1). It was reported that for GaN-based LEDs, ∼6% of light was emitted to air from the top surface of the LEDs, while ∼22% was trapped by total internal reflection and ∼66% was trapped to optical guided modes in the LEDs [25]. Improving light extraction efficiency is another area of research which attracted much attention from researchers in the past decades. Surface-patterned [26, 27, 28], flip-chip [29, 30], and photonic crystal LEDs [31, 32, 33] are examples of solid state LEDs with improved light extraction efficiency. Recently, photonic crystal GaN-based LEDs with 73% light extraction efficiency has been demonstrated [34].

Solid-state LEDs provide various light colours ranging from ultraviolet to infrared. The emission of InGaN/GaN QW LEDs, for instance, can be tuned from ultraviolet to green colour by increasing the indium composition or the thickness of the QWs. However, as increasing the indium composition and the thickness of the QWs, phase segregation of indium and lattice mismatch between InGaN and GaN degrade quality of the LEDs [35]. To achieve a broad spectrum of desirable colours, materials with different band gaps are needed to use as emissive layers of the LEDs, for example, GaAs, AlGaAs and GaP provide emission spectra ranging

from yellow to near-infrared colour while GaN, InGaN can be used in ultraviolet, blue and green regions.

An alternative way to produce multi-colour LEDs is to use hybrid structures of GaN-based LEDs and colloidal QD emitters. The GaN-based LED emits energetic photons which are subsequently absorbed by the QD emitters. The excited carriers in the QDs rapidly relax to the band edge and finally return to the ground states radiatively by emitting lower energy photons or nonradiatively via phonon scattering. Therefore, the colour of this colour-conversion LED can be simply chosen from size or material compositions of the QD emitters.

Having served as the main source for energy, non-renewable energy resources such as coal, petroleum and natural gas are depleted continuously. The lack of non-renewable energy resources may become a serious problem in the near future. Among various renewable energy sources such as wind, tidal waves and hydro power, solar power is a promising alternative. It was reported that the solar energy that struck the earth in one hour was enough for one year global energy consumption [36]. Many studies have been carried out in order to find efficient methods of using the solar power. Photovoltaic (PV) cells are the main devices being used to extract the energy from the solar radiation.

Due to the progress of chemical synthesis, colloidal QDs [37, 38] offer low-cost, solution-process, large area features to PV applications [39, 40, 41]. Owing to excellent optical properties of the colloidal QDs such as high absorption and wavelength tunability, there have been many attempts during the last decades to incorporate colloidal QDs into PV cells [42, 43, 44]. Although the thermodynamic

limit of a single band gap PV cell limits the cell efficiency to 31% [45], the efficiency of colloidal QD PV cells as high as 60% was proposed [46].

This thesis is focused on a study of resonant energy transfer in light emitting and light harvesting devices. The theories of resonant energy transfer, optical transitions and operating principles of light emitting and light harvesting devices are presented in Chapter 2.

Resonant energy transfer in a hybrid organic/inorganic heterostructure is optically studied in Chapter 3. By engineering the energy band of a GaAs single QW and organic dye emitters, optical excitation energy of the single QW can be transferred to the organic dye emitters via resonant energy transfer. The simultaneous increase of the QW population decay rate and the organic dye rise time provide conclusive evidence of resonant energy transfer in the hybrid structure. The combination of the GaAs single QWs and the organic dye emitters provides light emission in the near-infrared region.

Hybrid colour-conversion LEDs consisting of surfaced-patterned GaN-based LEDs and colloidal QDs are investigated in Chapter 4. Here, carriers are electrically injected to the LED and the excitation energy of the LED is transferred to the QD emitters whose emission is in the visible region. A twofold increase of the QD emission in this hybrid LED is achieved owing to resonant energy transfer.

In Chapter 5, hybrid structures of colloidal QDs and patterned semiconductor heterostructures are designed and fabricated to use in light harvesting applications. Excitation energy can be transferred from colloidal QDs with high absorption to a patterned semiconductor heterostructure possessing relatively high carrier mobility via resonant energy transfer. This configuration offers efficient light harvesting

devices where high absorption and wide spectrum of colloidal QDs are utilised while their low carrier transfer is circumvented.

Chapter 2

Theoretical Background

2.1 Interband transition

Interband transition of electronic states is a fundamental principle of many optoelectronic devices such as photodiodes, PV cells and LEDs. To form semiconductor crystals, isolated atoms with discrete energy levels are packed into a crystal structure. The atoms in the crystal are in close proximity to each other resulting in the overlap of the electron wave functions. Consequently, the degenerate energy levels are split due to the Pauli exclusion principle. The splitting leads to the formation of energy bands so called the valence band and the conduction band. For nondegenerate semiconductors where a low level of doping atoms is introduced, the valence band is fully occupied by electrons and the conduction band is empty at absolute zero temperature.

2.1.1 Absorption

For direct band gap semiconductors, the minimum of the conduction band and the maximum of the valence band are at the zone centre ($k = 0$) of the Brillouin zone. The band gap is determined by the energy difference of the energy bands at the zone centre. Photons with energy greater than the band gap can excite valence electrons to the conduction band. Since the momentum of photons is negligible compared to that of electrons, the wave vector of electrons remains the same after being excited from the valence band to the conduction band as shown by a straight arrow in figure 2.1. The transition rate is given by Fermi's golden rule:

$$W_{i\to f} = \frac{2\pi}{\hbar} |M|^2 \, g(\hbar\omega), \tag{2.1}$$

where M and $g(\hbar\omega)$ are the matrix element and the joint density of states respec-

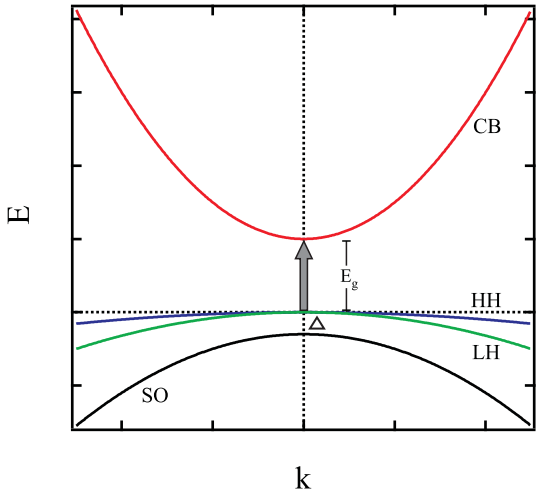

FIGURE 2.1: Energy band of bulk semiconductor materials. The heavy hole (HH) and light hole (LH) bands are degenerate at k=0. Δ is split-off energy of the split-off (SO) band

tively. The transition from p-like states of the valence band to s-like states of the

conduction band is allowed according to the selection rules of bulk semiconductors. Hence, the transition rate is proportional to the joint density of states and given by:

$$g(\hbar\omega) = 0 \text{ for } \hbar\omega < E_g, \tag{2.2}$$

$$g(\hbar\omega) = \frac{1}{2\pi^2}\left(\frac{2\mu}{\hbar^2}\right)^{3/2}(\hbar\omega - E_g)^{1/2} \ \ for\ \hbar\omega \geq E_g, \tag{2.3}$$

where the reduced mass is given by $\mu^{-1} = m_e^{-1} + m_h^{-1}$ and m_e and m_h are electron and hole effective mass respectively. There is no absorption for photons possessing energy less than the energy band gap ($\hbar\omega < E_g$) whereas the absorption scales with $(\hbar\omega - E_g)^{1/2}$ for $\hbar\omega \geq E_g$ as shown in figure 2.2.

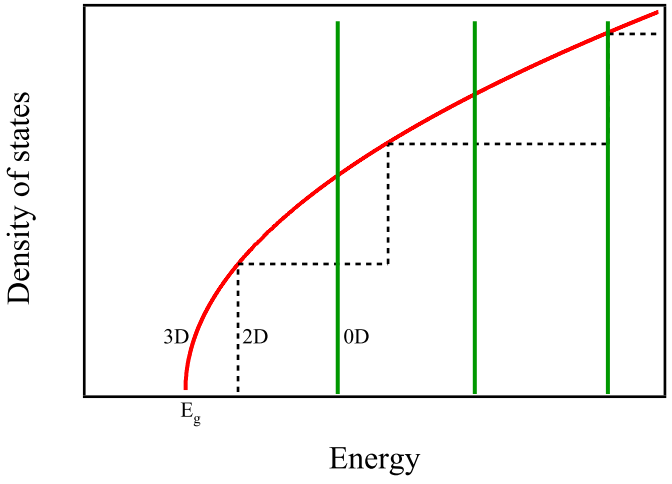

FIGURE 2.2: Density of states of bulk semiconductors (red solid line), QWs (black dashed line) and QDs (green solid lines)

Quantum confinement in semiconductors has influence on the characteristics of joint density of states and consequently the optical transition. While joint density of states of two-dimensional semiconductors or QWs has a step-like structure, that of zero-dimensional semiconductors or QDs has discrete structures.

2.1.2 Luminescence

After being excited to the conduction band, electrons rapidly relax to the lower energy states by emitting phonons. The phonons which are involved in each relaxation step have to satisfy conservation of energy and momentum. The electron-phonon coupling occurs in a short time scale (∼100 fs) compared to the radiative decay rate (∼1-10 ns in direct band gap semiconductors). Therefore, the excited electrons relax to the bottom of the conduction band and form thermal distribution before undergoing radiative decay. The same process applies to holes in the valence band. The thermalised carriers can also undergo nonradiative recombination via trap centres or phonon emission. If the nonradiative recombination rate exceeds the radiative recombination, little light will be emitted resulting in low quality LEDs. Quantum efficiency of solids is given by:

$$Q = \frac{k_r}{k_r + k_{nr}}, \tag{2.4}$$

where k_r and k_{nr} are radiative and nonradiative decay rate respectively. The quantum efficiency approaches 1 when the radiative rate is much more than the nonradiative rate ($k_r >> k_{nr}$).

The luminescence spectrum of semiconductors can be described by:

$$I(\hbar\omega) \propto |M|^2 \, g(\hbar\omega) f(\hbar\omega), \tag{2.5}$$

where $f(\hbar\omega)$ is the occupancy factor for the electron state in the conduction band and the hole state in the valence band. At low carrier densities, the distribution of electrons in the conduction band and that of holes in the valence band can be

approximated by Boltzmann statistics:

$$f(E) \propto e^{-E/k_B T}, \tag{2.6}$$

where k_B and T are Boltzmann constant and absolute temperature respectively. Hence, the luminescence spectrum from equation 2.5 is given by:

$$I(\hbar\omega) \propto (\hbar\omega - E_g)^{1/2} e^{-(\hbar\omega - E_g)/k_B T}, \tag{2.7}$$

The luminescence spectrum has a sharp rise at energy band gap described by the factor $(\hbar\omega - E_g)^{1/2}$ and followed with an exponential drop associated with the factor $e^{-(\hbar\omega - E_g)/k_B T}$. The spectral width can be approximated to be $\sim k_B T$.

2.2 Excitons

As a result of photon absorption, the interband transition creates an electron in the conduction band and a hole in the valence band. The electron and hole can bind together with Coulomb attraction and form excitons. Excitons can modify optical properties of materials such as absorption and luminescence. There are two types of excitons, Wannier-Mott excitons and Frenkel excitons.

2.2.1 Wannier-Mott excitons

Wannier-Mott excitons or free excitons are generally observed in semiconductor materials. The excitons can move freely in the crystals and encompass many unit cells ($\sim$50000 unit cells for GaAs). The bound electron-hole state can be approximately

described by Bohr model. The exciton energy is quantised and the binding energy of the nth level is given by:

$$E_n^b = -\frac{\mu}{m_0}\frac{1}{\epsilon_r^2}\frac{R_H}{n^2}, \tag{2.8}$$

where m_0 and ϵ_r are the electron rest mass and dielectric constant respectively. R_H is the Rydberg constant of hydrogen atoms ($R_H = 13.6$ eV). The exciton radius is also quantised and given by:

$$r_n = \frac{m_0}{\mu}\epsilon_r a_H n^2, \tag{2.9}$$

where a_H is the Bohr radius of hydrogen atoms ($a_H = 5.29 \times 10^{-11}$ m). The most stable excitons have maximum binding energy and minimum exciton radius at $n = 1$. Wannier-Mott excitons are observed below a certain temperature where the binding energy is greater than thermal energy ($\sim kT$). At temperature $kT > E_n$, excitons are dissociated and unbound electron-hole pairs are formed.

2.2.2 Frenkel excitons

Frenkel excitons or tightly bound excitons are typically found in alkali halide crystals and molecular crystals such as organic semiconductors. The excitons have higher binding energy and smaller exciton radius than Wannier-Mott excitons. Frenkel excitons are localised on the atoms at which they are created. Due to their high binding energy, for example LiF has $E_1^b = 1.9$ eV, Frenkel excitons can be observed at room temperature. Organic semiconductor microcavities utilise the high binding energy of Frenkel excitons to study the interaction of light and matter at room temperature [47, 48].

2.3 Quantum wells

When the dimensionality of bulk materials is decreased from three to two dimensions, many interesting phenomena such as quantum confinement of carriers emerge. Semiconductor quantum well (QWs), for instance, consist of a thin well layer with the thickness in the order of the de Broglie wavelength sandwiched between relatively higher band gap materials. The quantum confinement of carriers leads to the quantisation of energy in the direction perpendicular to the QW plane. In the case of infinite potential wells, the confinement energy of the quantum wells with thickness d is given by:

$$E_n = \frac{\hbar^2}{2\mu}\left(\frac{n\pi}{d}\right)^2. \tag{2.10}$$

Hence, the characteristics of the interband transitions including absorption and luminescence are modified. Particularly, the absorption threshold changes from E_g to $E_g + \frac{\hbar^2}{2\mu}\left(\frac{\pi}{d}\right)^2$ and the joint density of states become a step-like curve as shown in figure 2.2. The QW emission energy, therefore, can be controlled by varying the well thickness. The confinement energy in equation 2.10 is estimated from an infinite potential well model. In real QWs with finite potential wells, the wave functions can tunnel into the barriers resulting in reduced confinement energy.

2.4 Quantum dots

Quantum dots (QDs) are defined as structures that confine carriers in three dimensions and have different optical and electrical properties from bulk structures of the same material. QDs can be produced by various methods, for example lithography, epitaxial growth and chemical synthesis. In general, different types of QDs

are obtained from different techniques. Chemically synthesised colloidal QDs, for instance, offer excellent optical properties. In addition, the cheap, large scale and simple fabrication renders colloidal QDs as promising materials for efficient opto-electronic devices.

The electronic structure of QDs cannot be described by continuous bands as in bulk materials. It is that of discrete levels similar to the electronic structure of atoms or molecules. The three dimensional quantum confinement results in the increase of electron-hole overlap and subsequently the increase of radiative recombination rate. The emission energy of QDs can be controlled by either the QD size or the material composition. It was demonstrated theoretically [49, 50] and experimentally [51, 52] that the confinement of excitonic wave functions in QDs enhanced the oscillator strength by a factor of $(\frac{d}{r})^3$ where d and r are radii of the QDs and the excitons respectively. Therefore, QDs can be used as absorbers with giant oscillator strength in PV cells or emissive layers with excellent brightness in LEDs.

The ratio of surface atoms to inner atoms increases as the dimensionality of materials decreases from bulk to QDs. The interaction of surface atoms with the surrounding environment becomes significant and plays an important role in material properties. Particularly, surface states of colloidal QDs can trap carriers and cause nonradiative recombination which leads to poor quantum yield. Surfactants such as phosphines, phosphine oxide and amides are needed to passivate the surface states. Moreover, the surfactants provide the solubility of QDs in various solvents.

2.5 Organic semiconductors

Fundamental principles of organic semiconductor materials are different from those of inorganic materials discussed above. Optical transition of organic materials is based on the transition of isolated molecules where the electronics states are discrete levels. The constituent atoms in a molecule can vibrate about their bonds leading to discrete vibrational states in addition to the electronic states. Hence, the optical transitions of organic materials are associated with both electronic and vibrational states called vibronic transitions as shown in figure 2.3. Electrons from the constituent atoms fill the molecular orbital up to the highest occupied molecular orbital (HOMO) level. The first excited state energy level is defined as the lowest unoccupied molecular orbital (LUMO) level.

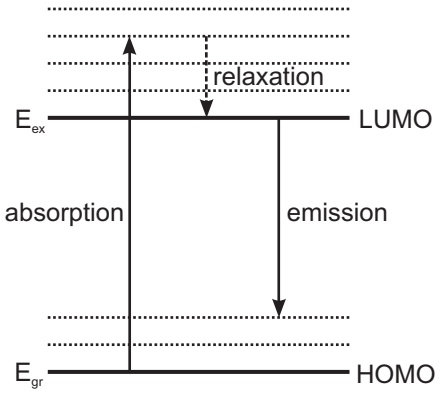

FIGURE 2.3: Schematic diagram illustrates optical transition of organic materials.

Energy of vibrational states can be described by quantum mechanics and given by $(n + 1/2)\hbar\Omega$ where n and Ω are the vibrational order and the angular frequency respectively. The optical transition from the vibrational order n_{gr} of the ground state to the vibrational order n_{ex} of the first excited state therefore requires

excitation energy: [53]

$$E_{excitation} = E_{ex} + \left(n_{ex} + \frac{1}{2}\right)\hbar\Omega_{ex} - E_{gr} + \left(n_{gr} + \frac{1}{2}\right)\hbar\Omega_{gr}, \tag{2.11}$$

where Ω_{ex} and Ω_{gr} are angular frequency of the vibrational excited state and the vibrational ground state respectively. The excitation rapidly relaxes to the bottom of the excited states by emitting phonons before returning to the ground state by emitting a photon. The absorption energy is normally higher than the emission energy except for the transition without the association of vibrational states. The difference of the absorption and the emission energy is referred to as *Stokes shift*.

2.6 Resonant energy transfer

Resonant energy transfer is a mechanism where excitation energy transfers nonradiatively from one molecule (donor) to another (acceptor). Several types of resonant energy transfer such as electric dipole-dipole interaction, electric dipole-quadrupole interaction and Dexter transfer have been theoretically and experimentally demonstrated [1, 54, 55]. Whereas electric dipole-dipole interaction or Förster energy transfer requires allowed transitions of both donors and acceptors, electric dipole-quadrupole interaction involves allowed transitions of the donors and forbidden transitions of the acceptors. The transfer rate of the former is consequently higher. Since Dexter transfer requires the overlap of the donor and the acceptor wave functions the transfer can occur only in a short distance, typically in the order of 15-20 Å. As the donor-acceptor separation distance of the systems studied here is greater

than the Dexter transfer length, this thesis will focus on the electric dipole-dipole interaction.

For dipole-dipole interactions, there is no real photon involved in the transfer process unlike radiative energy transfer where the photons emitted from donors are reabsorbed by acceptors. It has been reported that resonant energy transfer is more efficient than conventional radiative energy transfer commonly used in typical colour-conversion LEDs [4, 13]. Resonant energy transfer has been used in various applications such as light harvesting devices [56, 57, 58, 59], multi-colour LEDs [60, 61, 62] and fluorescent tags in biological cells [63]. First studied in molecular systems [1, 64], resonant energy transfer has been widely investigated in other systems, for example, organic/inorganic heterostructures [65, 66] and colloidal QD/inorganic heterostructures [5, 67]. A schematic diagram of resonant energy transfer process in a molecular system is shown in figure 2.4.

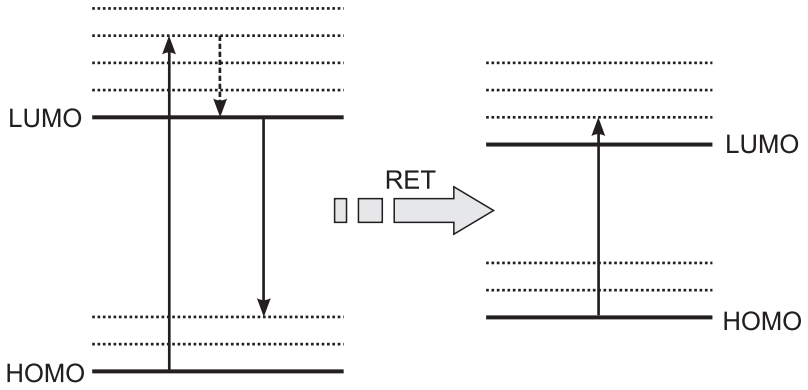

FIGURE 2.4: Schematic diagram illustrates resonant energy transfer.

Resonant energy transfer requires the overlap between the donor emission and the acceptor absorption and the appropriate separation distance between the

donor and the acceptor as the transfer rate is inversely proportional to the separation distance. For molecular systems illustrated in figure 2.4, a donor molecule is excited from the ground state or the HOMO level to an excited state with the excess energy which is simultaneously converted into vibrational energy. The molecule relaxes rapidly within 0.1-1 ps to the LUMO level through heat dissipation and may return to the ground state radiatively by emitting a photon or nonradiatively via phonon scattering. Provided there is a nearby molecule (acceptor) whose absorption overlaps with the donor emission, the coupling of the transition dipoles of the donor and the acceptor may lead to the transfer of the excitation energy from the donor to the acceptor via resonant energy transfer.

According to Förster's theory, the resonant energy transfer rate (k_{ET}) in molecular systems is given by the following equation,

$$k_{ET} = k_D \left(\frac{R_0}{R}\right)^6, \tag{2.12}$$

where k_D is the decay rate of the donor and R is the separation distance between the donor and the acceptor. Förster critical distance (R_0) is the separation distance where the resonant energy transfer efficiency (η_{ET}) is 50% and defined by the following equation (in nm),

$$R_0 = 2.11 \times 10^{-2} \left(\frac{\kappa^2 \Theta Q_D}{n^4}\right)^{1/6}. \tag{2.13}$$

The orientation factor (κ) is associated with relative orientation of the donor and the acceptor dipoles. κ^2=0 and 4 correspond to the perpendicular and the parallel

transition dipoles respectively. Q_D is quantum yield of donors, n represents refractive index of the medium and Θ is spectral overlap between the donor emission and the acceptor absorption as shown in figure 2.5. The resonant energy transfer efficiency is given by,

$$\eta_{ET} = \frac{k_{ET}}{k_{ET} + k_D}. \tag{2.14}$$

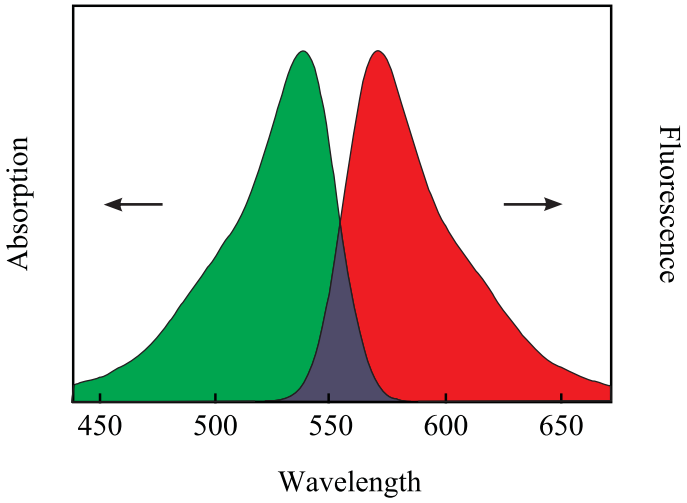

FIGURE 2.5: Spectral overlap of the donor emisson and the acceptor absorption.

The resonant energy transfer rate also depends on the dimensionality of the involved electronic excitations. Whereas k_{ET} is proportional to R^{-6} in the case of isolated dipoles, k_{ET} scales with R^{-4} for the transfer from an isolated dipole to a layer of acceptors and R^{-2} for the transfer between two layers [1, 4, 9].

Resonant energy transfer can be observed from the quenching of the donor emission in the presence of acceptors. Alternatively, resonant energy transfer efficiency can be determined from the luminescent intensity of the donor: [68]

$$\eta_{ET} = 1 - \frac{I_D^H}{I_D}, \tag{2.15}$$

where I_D^H and I_D are the donor luminescent intensity with and without the presence of the acceptor respectively.

2.7 Light emitting devices

Light emitting devices (LEDs) are optoelectronic devices that convert electrical current into photons. LEDs were initially used for indicator light due to their low efficiency and few choices of the colours. The technology of LEDs has been continuously developed leading to efficient LEDs with broad spectra including ultraviolet, visible and infrared regions [69, 70, 71, 72]. At present, LEDs are widely used in various optoelectronic applications such as displays, lighting and other electronic devices. One of the highest efficiency LEDs at the present from Cree, Inc. has 173 lumen of light output and 161 lumen/watt efficacy at 350 mA [73] compared to incandescent light bulbs (∼15 lumen/watt) and fluorescent lamps (∼100 lumen/watt).

In inorganic semiconductor LEDs such as blue GaN-based LEDs and red-GaAs based LEDs, the operating principle is based on p-n junctions. Electron and holes are electrically injected from the corresponding electrodes, transport to the junction and recombine radiatively. The energy of the emitted photons is associated with the band gap of the active materials. LEDs made of direct band gap materials such as GaAs and GaN has higher efficiency than the very first LEDs made of indirect band gap mateirals because phonon scattering is involved in the recombination process of the indirect band gap materials.

In spite of the high efficiency of inorganic semiconductor LEDs, the fabrication process is associated with complex techniques and the requirement of high

quality materials which lead to expensive devices. Alternatively, organic LEDs (OLEDs) have been developed and demonstrated low cost, large area, flexible devices [74, 75, 76, 77]. In addition, the efficacy of OLEDs is currently comparable to incandescent light bulbs and fluorescent lamps (102 lumen/watt, Universal Display Corporation [78]). In OLEDs, electrons and holes are electrically injected into the emissive layer by the corresponding electron and hole transport materials. The emission energy of the OLEDs is associated with the energy bands of the emissive materials.

OLED have been used in many electronic devices such as mobile phones, music players and digital watches. Recently, commercial 11-inch OLED televisions with outstanding contrast, high brightness and an ultra thin screen (3 mm) were launched [79]. In contrast to liquid crystal displays (LCDs), OLED displays do not need any backlight resulting in thinner screens as well as less power consumption. For lighting application, OLEDs with efficiency, lifetime and colour rendering index (CRI) comparable to or better than commercial fluorescent and incandescent lamps have been successfully demonstrated [80] as shown in table 2.1. CRI is an indicator of a light source to render the true colour of the objects being lit by the light source. Ideal light sources generally have CRI value close to 100 whereas monochromatic light sources have CRI value close to zero. For interior lighting applications, CRI value should be more than 70.

Although organic semiconductor materials have high potential in display and lighting applications, an inherit drawback of organic materials that hampers the device efficiency is known as their low carrier transfer [81, 82]. Moreover, charge imbalance in the emissive layer resulting from different charge transfer efficiency of

Light Source	Efficiency (lm/W)	CRI	Lifetime (h)
Incandescent lamp	10-15	>90	1,000
Fluorescent lamp	40-80	70	10,000
Light-emitting devices	>80	80	>10,000
Organic light-emitting device	65	>90	10,000

TABLE 2.1: Efficiency, colour rendering index (CRI) and lifetime of lighting devices.

the hole and the electron transport layers leads to low efficiency of the devices [83, 84]. A route to circumvent these problems is to combine organic materials with inorganic semiconductor materials which have relatively high carrier mobility into a hybrid structure. In the hybrid structures, carriers are electrically injected and transport in the inorganic semiconductor counterpart. The injected carriers are subsequently transferred in a noncontact way to the organic emitters via resonant energy transfer. The organic emitters eventually emit photons with desirable colours. The same method can be applied to colloidal QDs which have low carrier transfer. Owing to the tunability of colloidal QDs emission, hybrid structures of inorganic semiconductors and colloidal QDs offer efficient colour-conversion and white LEDs.

2.8 Photovoltaic cells

Photovoltaic (PV) cells are optoelectronic devices that convert solar energy into electrical current. The essential operating principles of PV cells consist of charge generation, charge separation and charge transport.

Charge generation. As photons from sunlight reach PV cells, the photons may reflect from the surface, be absorbed by the active materials or pass through the PV cells depending on the photon energy and the physical properties of the PV cells. Photons with energy less than the energy gap of the active materials can transmit through the PV cell whereas photons with energy higher than the energy gap can be absorbed resulting in photogenerated electron-hole pairs. The photon reflection and transmission lead to loss of charge generation and consequently low PV cell efficiency. Antireflection coating or surface texture layer can be used to increase the number of photons coupled into PV cells. The active layer has to be thick enough in order to absorb all the incident photons. Alternatively, highly absorbing materials such as colloidal nanocrystal quantum dots can be used as the active layer.

Charge separation and charge transport. Photogenerated electron-hole pairs in the active materials will contribute to electrical current if they are separated and collected by the corresponding electrodes. In p-n junction PV cells such as crystalline Si PV cells, photogenerated electron-hole pairs are separated by the internal electric field across the p-n junction. In organic PV cells, photogenerated carriers dissociate at the interface of electron and hole transport materials due to the energetic preference to the different energy bands of the corresponding transport materials. Historically, there have been three generations of PV cells [85].

First generation PV cells

First generation PV cells are based on single p-n junction PV cells of crystalline Si. These PV cells currently occupy over 80% of the market and have relatively high efficiencies, i.e. 12%-16% for commercial modules and ∼25% for

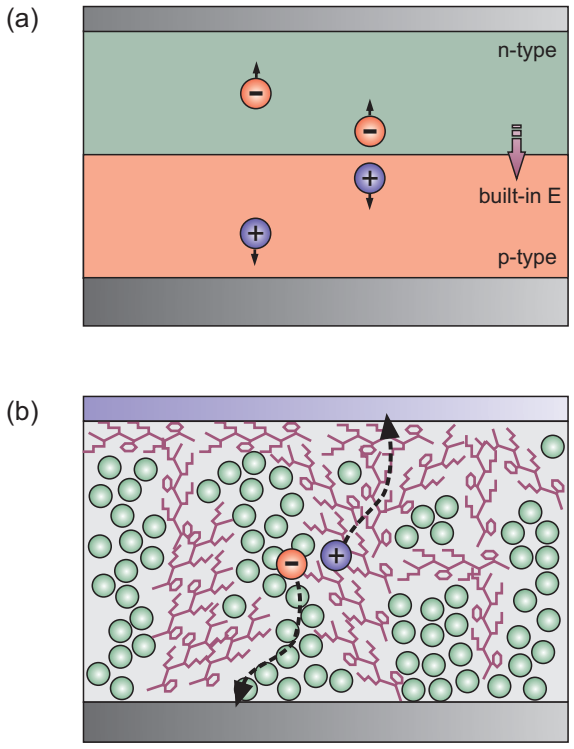

FIGURE 2.6: Charge generation and charge separation in (a) p-n junction PV cells (b) organic PV cells .

laboratory prototypes. However, the manufacturing processes associated with this generation of PV cells involve high technology, complicated production steps and large amount of high quality crystalline Si resulting in expensive PV cells.

Second generation PV cells

Thin films with high absorption such as $CuInSe_2$, $CuInGaSe_2$ and CdTe are developed and used as absorbing layers in the second generation PV cells. By using thin film technology, small amount of materials is needed in the manufacturing process resulting in cheaper PV cells. The efficiency of thin-film PV cells has been reported to be 8%-12% for modules and ~18% for laboratory cells which is lower than that of crystalline Si PV cells. In spite of the lower price, the relative low

efficiency of thin-film PV cells cannot decrease the value of price per unit current. The next generation of PV cells, therefore, are of high performance PV cells with the reduction of price per unit current.

Third generation PV cells

New concepts of high efficiency thin-film PV cells are developed in third generation PV cells. For instance, tandem cells with multiple junctions of different energy gaps covering wide absorption spectrum achieve the cell efficiency exceeding thermodynamic limit of single band gap PV cells of 31%. Recently, GaInP/-GaInAs/Ge multiple junction PV cells was demonstrated to have efficiency over 40% [86].

Alternatively, organic semiconductors and colloidal QDs offer low-cost, solution-process, and flexible PV cells [87, 88, 89]. In particular, there have been numerous efforts during the past decades to integrate colloidal QDs into PV cells owing to excellent optical properties of colloidal QDs such as high absorption and wide absorption spectrum. However, an inherent drawback of low carrier transport is a major problem that limits the efficiency of QD based PV cells [90, 91].

Power conversion efficiency (η) is a standard parameter used to indicate the performance of PV cells. The efficiency is defined by the ratio of the output power of the cells to the input power of the solar radiation (P_{in}). In order to compare the efficiency of different PV cells, the conditions under which the cell efficiency is measured need to be controlled. Power conversion efficiency of a PV cell is typically determined from its current-voltage characteristic under illumination. From a current-voltage characteristic in figure 2.7, the current at zero applied voltage is defined as the short circuit current (I_{sc}) and the voltage at zero current is defined

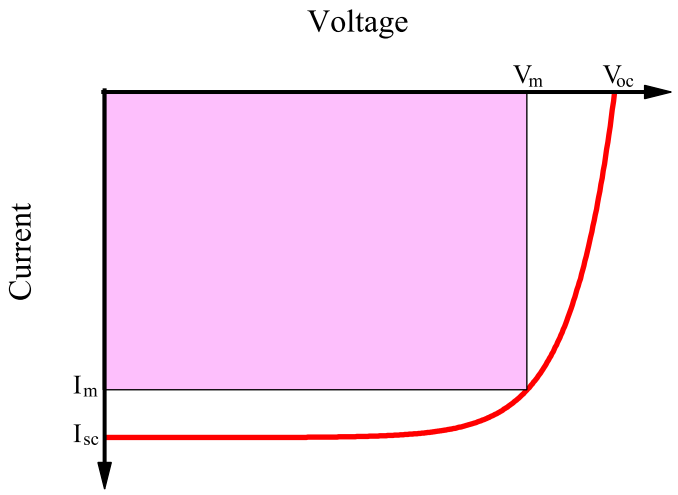

FIGURE 2.7: Current-voltage characteristic of a PV cell

as the open circuit voltage (V_{oc}). The fill factor (FF) is the ratio of the maximum power of the cells to the product of I_{sc} and V_{oc},

$$FF = \frac{I_m V_m}{I_{sc} V_{oc}}, \tag{2.16}$$

where I_m and V_m are the current and the voltage at which the cell gives the maximum power. Graphically, the fill factor represents the squareness of a current-voltage characteristic. Power conversion efficiency is given by

$$\eta = \frac{FF \cdot I_{sc} V_{oc}}{P_{in}}. \tag{2.17}$$

Chapter 3

Resonant Energy Transfer in Hybrid Organic/Inorganic Heterostructures

Wannier-Mott excitons in semiconductors and Frenkel excitons in molecular crystals have different characteristics. Whereas the interaction between Wannier-Mott excitons leads to interesting effects such as optical nonlinearlities, Frenkel excitons occupy large oscillator strength. It was theoretically proposed that the coupling of both types of excitons could create a hybrid electronic excitation possessing specific advantages of the individual components [92]. There have been attempts to couple Wannier-Mott excitons with Frenkel excitons in the strong coupling regime by using microcavity [93, 94]. Another way to couple the excitons of different classes of materials is to utilise resonant energy transfer in hybrid structures.

In this chapter, resonant energy transfer in hybrid organic/inorganic heterostructures is optically investigated. Whereas organic dyes used here are renowned as efficient light emitters, GaAs heterostructures have high carrier mobility. The integration of these materials can be used in light emitting devices or displays where carriers are electrically injected into the heterostructure and efficiently transferred to the organic emitters. For devices based on this hybrid configuration, low charge transfer of the organic dyes is overcome while benefiting their large oscillator strength.

3.1 Pump-probe reflection technique

A schematic diagram of a pump-probe reflection setup is shown in figure 3.1. An argon ion laser is used to pump a mode-locked Ti:sapphire oscillator which has a repetition rate of 76 MHz and a pulse width of $\sim$2 ps. The output of the mode-locked Ti:sapphire oscillator is initially split into two paths. The first path is used as a pump beam and the other is used as a probe beam. A polarised beam splitter (PBS) and a half wave plate ($\lambda/2$) are used to change the intensity ratio between the pump and the probe beams. After transmission through the PBS, the pump beam is passed through the inner holes of an optical chopper which rotate at frequency f_1. The pump beam is subsequently focused onto the sample by L6.

After reflection from the PBS, the probe beam is directed to a retroreflector which is fixed on a computer controlled translation stage. The delay time between the pump and the probe paths can be varied by changing the position of the translation stage. The probe beam is then passed through the outer holes of the optical chopper which rotate at frequency f_2 and eventually focused onto the sample. Part

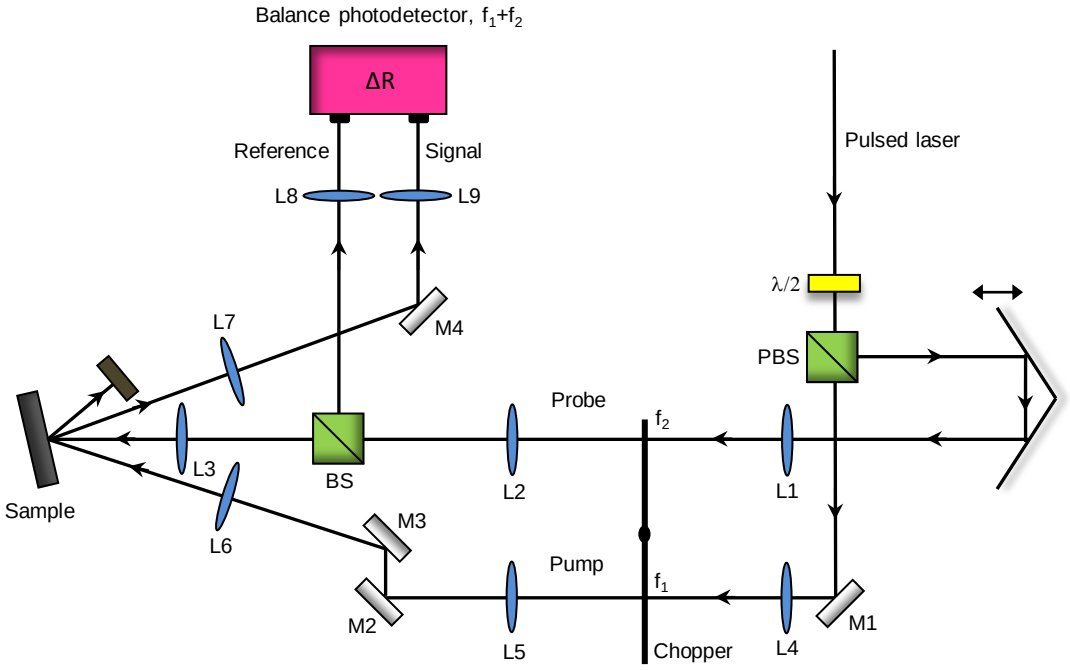

FIGURE 3.1: Pump-probe reflection setup.

of the probe beam is collected by a beam splitter (BS) and focused onto a balance photodetector (BD) to use as a reference beam. The transmitted probe beam is subsequently focused onto the sample where the probe spot overlaps with the pump spot. The reflected probe beam from the sample is collimated by L7 and directed to another photodiode of the balance photodetector. A tunable neutral density filter is used to balance the intensity of the reference and the reflected beams while the pump beam is blocked. The output of the balance photodetector is sent to a lock-in amplifier to detect the pump-induced change of reflectivity at the sum frequency (f_1+f_2).

In pump-probe reflection spectroscopy, the carrier population in the conduction band of semiconductors such as GaAs can be related to the reflected probe

intensity as shown in figure 3.2. At zero delay time, the pump pulse arrives the sample and excites carriers from the valence band to the conduction band. At later time t_1, some carriers in the conduction band relax to the valence band. Therefore, the number of valence band carrier at time t_1 is more than that at time t_0. If a probe pulse arrives the sample at t_1, a fraction of the probe pulse will be absorbed and the remaining fraction will be reflected. The same situation happens at time t_2 except for the larger fraction of the probe being absorbed. The probe pulse is absorbed with larger fraction at time t_2 because more carriers relax to the valence band at time t_2. By observing the intensity of the reflected probe beam as a function of the delay time, the information of carrier population decay in the conduction band can be obtained.

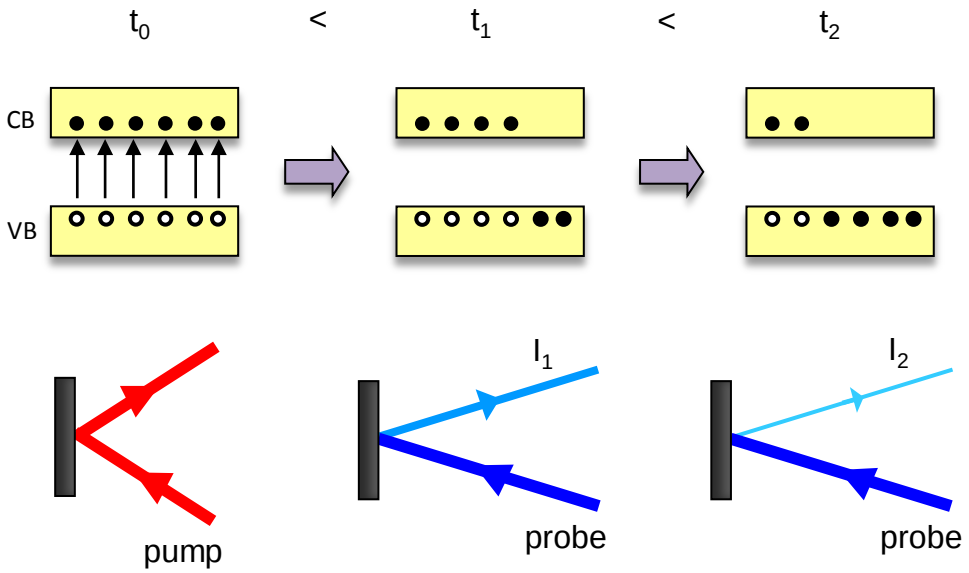

FIGURE 3.2: Principle of pump-probe reflection spectroscopy.

3.2 Time-correlated single photon counting measurements

Time-correlated single photon counting (TCSPC) is an optical technique widely used to study photoluminescence decays of materials. The operating principles of TCSPC are based on the detection of single photon signals, the accurate measurement of time interval between two detection pulses, and the reconstruction of photon distribution of the photoluminescence decay. Photomultiplier tubes (PMTs) or avalanche photodiodes (APDs) can be used as a photon detector providing pulses of single photons for a TCSPC module installed in a computer. The TCSPC module typically consists of three main units, i.e. constant fraction discriminators (CFDs), time-to-amplitude converters (TACs) and analog-to-digital converters (ADCs). The electronic pulses of single photons detected by PMTs or APDs are sent to the CFD unit. The pulses with amplitudes smaller than the threshold or higher than the upper limit are filtered out to remove noises from the detection. Another CFD is used to detect pulses from the excitation light source providing the reference signal. The reference and the photon signals from the CFDs are used to start and stop the TAC unit by switching on and off a current source applied to a capacitor. Therefore, the time interval between the reference and the photon signals is determined by the capacitor voltage. The output of the TAC unit is digitised by an ADC and converted to the detection time of the detected photons.

Time-correlated single photon counting is subjected to single photon detection of periodic photoluminescence decays obtained from pulse excitation. The photon detection rate should be low enough so that there is no more than one photon detected in an excitation period as shown in figure 3.3. There are some

periods that photons are not detected. The detection time of each photon is continuously recorded during the acquisition period and the distribution of the photon probability is subsequently produced.

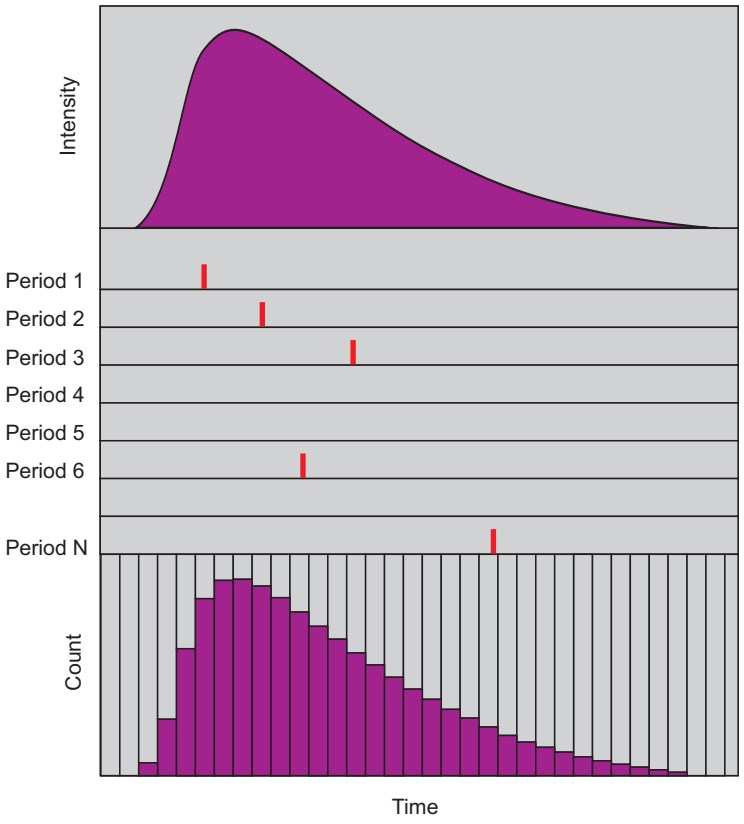

FIGURE 3.3: Photon probability distribution measured by time-correlated single photon counting.

Schematic of the TCSPC setup used here is shown in 3.4. A Ti:sapphire oscillator with a repetition rate of 76 MHz and a pulse width of ∼2 ps is used as an excitation source. The laser beam is initially split by a beam splitter and the first path is directed to a photodiode. The signal from this photodiode is used as the reference signal. The second path is used to excite the sample held in a closed cryostat. The photoluminescence of the sample is collected and passed through a monochromator to spectrally resolve the spectrum. The photoluminescence signal

is then focused onto an APD. The signal from the APD is then sent to a TCSPC module.

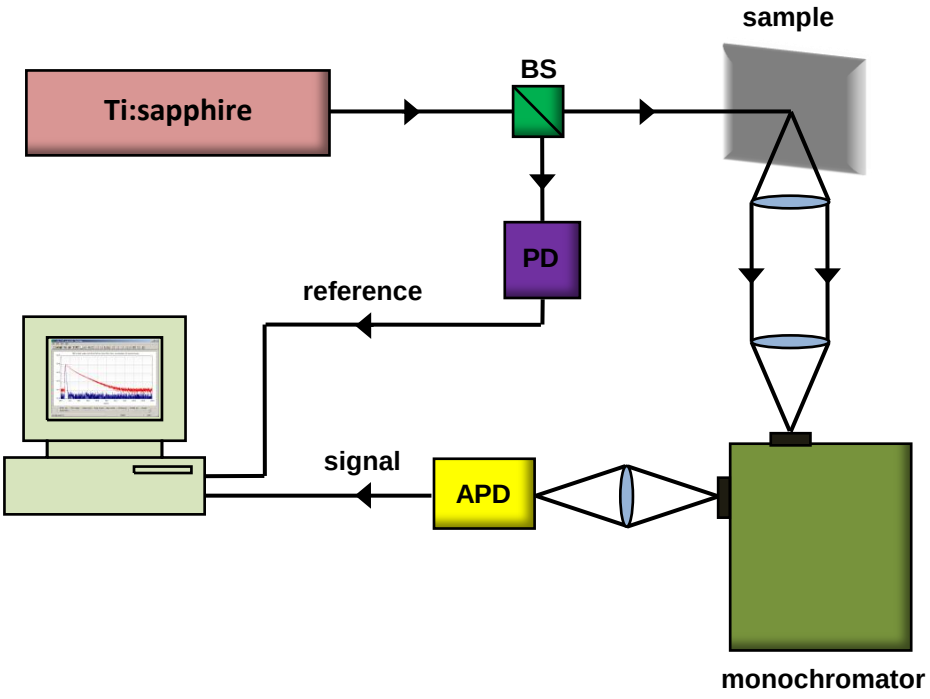

FIGURE 3.4: Time-correlated single photon counting setup.

3.3 Materials and methods

Figure 3.5(a) presents a schematic diagram of a hybrid organic/inorganic heterostructure consisting of a thin layer of cyanine dyes deposited on a GaAs single QW. The single QW is grown on a (100) GaAs substrate by molecular beam epitaxy (MBE). A 500 nm thick GaAs buffer layer is initially grown on the substrate followed by a 20 nm thick barrier of $Al_{0.35}Ga_{0.65}As$. The thickness of the wells is 4.0 nm and 6.5 nm for sample A and sample B respectively. Finally, both samples are capped with 7.5 nm thick $Al_{0.35}Ga_{0.65}As$ layers.

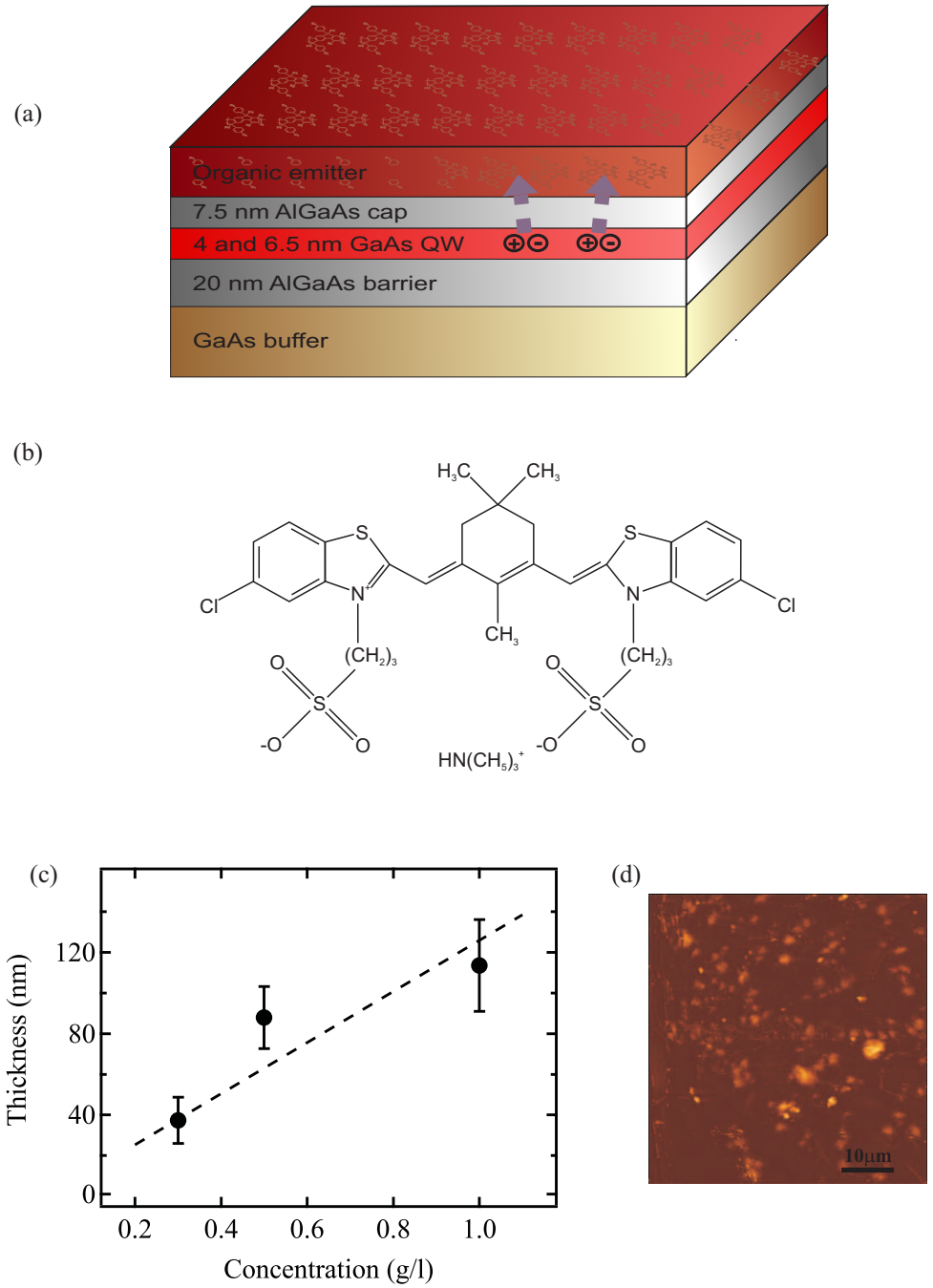

FIGURE 3.5: (a) Schematic diagram of the hybrid organic/inorganic heterostructure. (b) Chemical structure of organic dyes. (c) Film thickness dependence on the concentration of the organic dye solution. (d) Atomic force microscope image of the organic dye film.

The cyanine dyes [95], 3-[(2Z)-5-chloro-2-{[(3E)-3-{[5-chloro-3-(3-triethylammonium-sulfonatopropyl)-1, 3-benzothiazol-3-ium-2-yl]methylene}-2,5,5-trimethylcyclohex-1-en-1-yl]methylene}-1,3-benzothiazol-3(2H)-yl] propane-1-sulfonate, are synthesised by the interaction of two equivalents of 3-(5-chloro-2-methyl-1,3-benzothiazolium-3-yl) propane-1-triethylammonium-sulfonate with one equivalent of 1,3-diethoxy-2,5,5-trimethyl-1,3-cyclohexadiene at 145-150 °C in the presence of triethylamine. The chemical formula of the cyanine dyes is $C_{37}H_{49}Cl_2N_3O_6S_4$ with a molecular weight of 831.6 g/mol. The chemical structure of the cyanine dyes is shown in figure 3.5(b). The cyanine dyes are dissolved in methanol and spin coated on the QWs. Cyanine dyes possessing a self-association of the molecules generally form an extended J aggregate structure. In-line ordering of dipoles results in a band of delocalised states and only the lowest states have allowed transitions to the ground state. This leads to a red-shifted and narrowed absorption peak compared to that of the isolated molecules. The thickness of the organic film is controlled by the concentration of the organic dyes in methanol as shown in figure 3.5(c). Figure 3.5(d) shows a uniform organic dye film of nominal 12 nm thickness.

Time-resolved carrier dynamics of the single QWs are investigated by using pump-probe reflection spectroscopy described above. The single QWs are excited resonantly at the n=1 heavy-hole excitonic absorption by a tunable mode-locked Ti:sapphire oscillator. Time-resolved photoluminescence decay of the organic dyes is measured by using time-correlated single photon counting (TCSPC) technique together with a monochromator and appropriate optical filters to spectrally resolve the spectra. The organic dyes are excited at 745 nm at 25 K.

3.4 Results and discussions

The spectral overlap between the QW emission and the organic dye absorption is shown in figure 3.6. Sample A and B have emission peaks at 772 nm and 795 nm respectively at 25 K. The capping layer thickness of sample A and B is kept constant while the spectral overlap of the two samples are varied by changing the thickness of the wells or the QW emission energy. Hence, the dependence of the energy transfer rate on the spectral overlap can be investigated in this experiment.

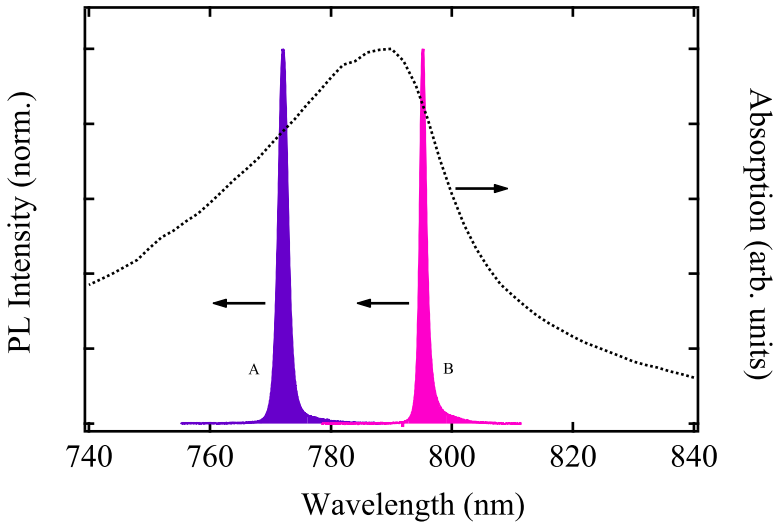

FIGURE 3.6: Spectral overlap of the hybrid organic/inorganic heterostructure. Sample A and B have photoluminescence peaks at 772 nm and 795 nm respectively at 25 K. The dotted line presents the organic dye absorption.

3.4.1 Resonant energy transfer at donor site

Due to the broad spectrum of the cyanine dye emission as well as its overlap with the QW emission, it is difficult to resolve the spectra of the cyanine dyes and the QW from the hybrid structures. Therefore, pump-probe reflection spectroscopy is used

to observe the QW carrier dynamics in the hybrid structures. Figure 3.7 presents the QW population decays of sample A and B with and without the deposited dye layers where the excitation wavelengths for sample A and B are 768 nm and 792 nm respectively.

Evidently, the population decay rate of the QW in the presence of the organic overlayer (k_{QW}^{H}) is greater than the decay rate of the bare QW counterpart (k_{QW}) for both samples. The decay rate increases from 3.1 ns^{-1} to 4.3 ns^{-1} for sample A and from 1.6 ns^{-1} to 2.6 ns^{-1} for sample B after the dye deposition. The faster decay rate indicates an extra decay channel from the QW to the cyanine dye overlayer via resonant energy transfer. Hence, the decay rate of the QW in the hybrid structure is given by $k_{QW}^{H} = k_{QW} + k_{ET}$. The efficiency of resonant energy transfer, $\eta_{ET} = k_{ET}/(k_{ET} + k_{QW})$, of sample A and B is 0.23 and 0.39 respectively.

Since the energy transfer rate scales linearly with the spectral overlap, the ratio of the energy transfer rates obtained from sample A and B k_A/k_B is expected to be equal to the ratio of the spectral overlap Θ_A/Θ_B. From the experiment above, $k_A/k_B = 1.18 \pm 0.21$ is determined and $\Theta_A/\Theta_B = 1.27$ is calculated from the spectral overlap in figure 3.6. The two values are in agreement and therefore provide further confirmation of the nature of resonant energy transfer in the hybrid structures as well as the validity of the pump-probe spectroscopy used in this experiment.

3.4.2 Resonant energy transfer at acceptor site

The faster QW population decay in the hybrid structure is a good indication of resonant energy transfer. However, only carrier dynamics in the QW may not fully verify the existence of resonant energy transfer as the deposited dyes could modify

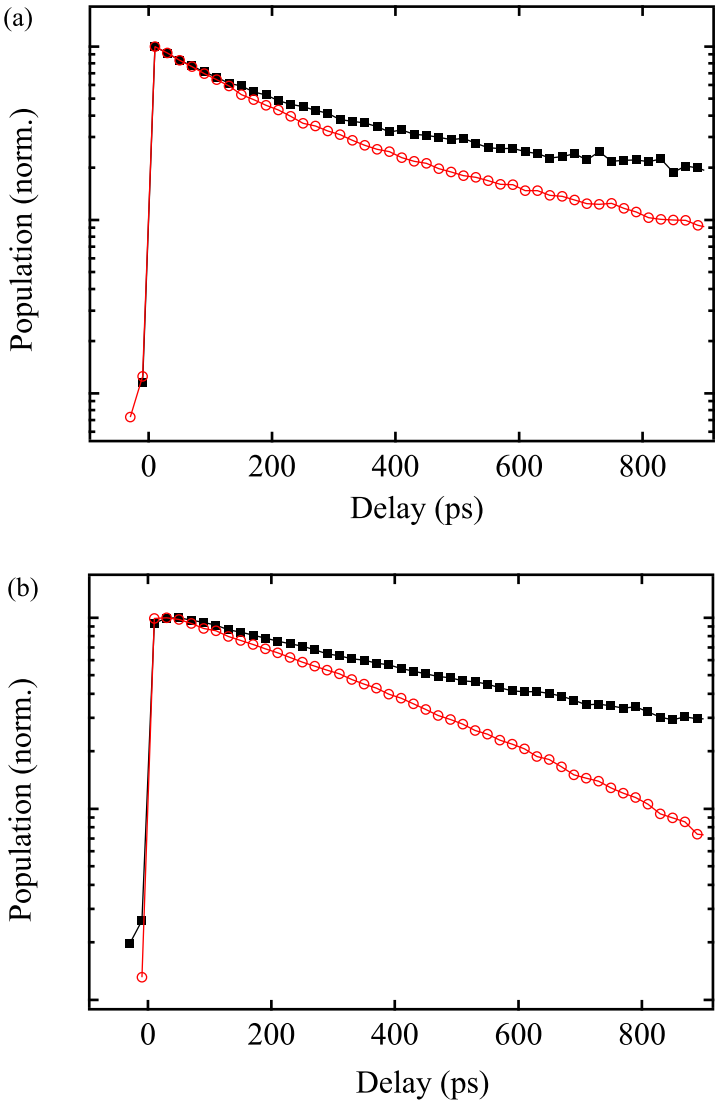

FIGURE 3.7: Normalised population decays of the single QWs with (red open circles) and witout deposited the cyanine dyes (black solid squares) for (a) sample A and (b) sample B.

the QW surface states leading to the alteration of the QW carrier dynamics. In order to confirm the occurrence of resonant energy transfer in the hybrid structures, time-resolved photoluminescence decay of the cyanine dyes is investigated by using TCSPC. A mode-locked Ti:sapphire oscillator tuned to 745 nm is used as an excitation source. The photoluminescence decay of cyanine dyes deposited on a glass substrate is measured and shown in figure 3.8. Since there is no effect of resonant energy transfer in this system, the photoluminescence decay illustrates intrinsic carrier dynamics of the cyanine dyes which have biexponential decay characteristics. The fast and slow components of the photoluminescence decay are attributed to the decay from aggregates of the dye molecules and from uncoupled monomers respectively. The photoluminescence decay of cyanine dyes deposited on sample A is measured and compared to the decay of cyanine dyes deposited on a glass substrate. Evidently, the rise time of the former is slower suggesting resonant energy transfer from the QW to the organic dye overlayer.

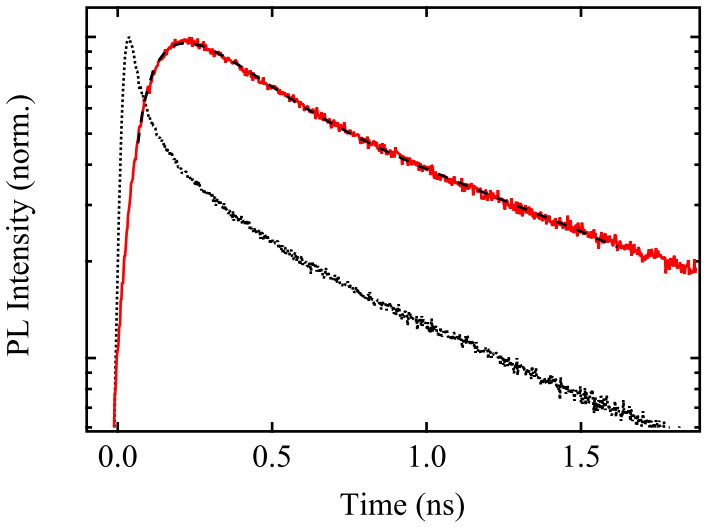

FIGURE 3.8: Fluorescence decays of the organic dye deposited on a glass substrate (black dotted line) and on sample A (red solid line). The dashed curve is the fit using equation 3.3.

To further explore the effects of resonant energy transfer on carrier dynamics of the hybrid structures, a kinetic model is established and described by the following equations:

$$\frac{dN_{QW}}{dt} = -k_{QW}N_{QW} - k_{ET}N_{QW}, \tag{3.1}$$

$$\frac{dN_{OGi}}{dt} = -k_{OGi}N_{OGi} + k_{ET}N_{QW}, \tag{3.2}$$

where i=1 and 2 present the fast and slow components of the organic photoluminescence decay. N_{QW} and N_{OGi} are exciton populations in the QWs and the cyanine dyes respectively. The fast (k_{OG1}) and slow (k_{OG2}) decay rates of cyanine dyes are derived from the experimental data. The analytic solution of the above equations is given by:

$$I(t) = \sum_{i=1,2} \frac{C_i N_{QW}(t=0)k_{ET}}{k_{OGi} - k_{QW} - k_{ET}} \left(e^{-(k_{QW}+k_{ET})t} - e^{-k_{OGi}t}\right), \tag{3.3}$$

where C_1 and C_2 are constants. This solution can describe carrier dynamics of organic dyes in the hybrid structure as shown by the black dashed line in figure 3.8. Table 3.1 shows the fixed parameters used in the fit. The fit shows a good agreement between the kinetic model and the experiment data.

Parameter	Value (ns^{-1})
k_{QW}	3.1
k_{OG1}	10.0
k_{OG2}	0.8
k_{ET}	1.2

TABLE 3.1: Parameters used in the fit of the organic photoluminescence decay in the hybrid structure.

3.5 Conclusions

Organic semiconductor materials provide bright, flexible, low-cost and full colour light emitters. However, a major problem of the organic light emitters that limits the efficiency of organic optoelectronic devices is their poor carrier transfer. In this study, hybrid structures of organic dyes and inorganic semiconductor heterostructures are investigated. The hybrid structure utilises high carrier mobility of inorganic semiconductor QWs while still benefits the high brightness of organic light emitters. In the hybrid structure, the energy of the optical excitation in the QW is transferred to the organic overlayer via resonant energy transfer with efficiency higher than traditional radiative energy transfer.

Conclusive evidence of resonant energy transfer is demonstrated at the donor and acceptor sites. The faster QW population decay in the hybrid structure compared to that of the bare QW counterpart indicates an extra decay channel of resonant energy transfer which is in good agreement with the slower rise time of the transient photoluminescence decay of the organic emitters when deposited on the QW. Moreover, the photoluminescence decay of the organic overlayer can be described by a kinetic model of carrier dynamics in the hybrid structure taking into account the effect of resonant energy transfer.

The hybrid structure offers a novel route of pumping organic light emitters which can lead to highly efficient OLEDs or organic lasers. In the next chapter, hybrid colour-conversion LEDs will be discussed where carriers are electrically injected into a surface-patterned semiconductor heterostructure and the excitations are transferred to adjacent QD emitters via resonant energy transfer. In chapter 5, a

reverse configuration of the hybrid structure is explored for using in light harvesting applications.

Chapter 4

Enhanced Colour-conversion Efficiency in Hybrid Light Emitting Devices

Conventional colour-conversion LEDs are typically based on the combination of blue LEDs and colour-tunable light emitters such as phosphorescent materials. Owing to the excellent optical properties and the simple synthesis process of colloidal QDs, they have rapidly become prominent alternatives for light emitter materials. Excitations in a blue LED (donors) are transferred to light emitters (acceptors) via radiative energy transfer where photons initially emitted by a blue LED are absorbed by colour-tunable light emitters. The emitters then reemit photons with lower energy. Nevertheless, the efficiency of radiative energy transfer is relatively low, <10%, due to several energy loss steps in the transfer process such as the waveguide mode confinement in blue LEDs.

By engineering the spectral overlap between the donor emission and the acceptor absorption as well as designing the structure of colour-conversion LEDs, efficient resonant energy transfer can be additionally utilised leading to higher performance LEDs. Resonant energy transfer rate (k_{ET}) is proportional to R^{-C} where R is donor-acceptor separation distance and C is a constant describing characteristics of the system. For example, $C = 2$ and 6 describe energy transfer in layer-layer and isolated dipole-dipole systems respectively [9, 96]. In order to increase the energy transfer rate, the donor-acceptor separation distance has to be minimised [13, 97]. For a hybrid colour-conversion LED consisting of emissive materials deposited on the surface of a heterostructure LED, the upper contact layer has to be as thin as possible to have maximum energy transfer rate, while remaining the appropriate thickness in order to have uniform spread of injected carriers.

In this chapter, resonant energy transfer in a hybrid colour-conversion LED consisting of colloidal QDs and a surface-textured LED is investigated. Hole structures with elliptical cross-section are fabricated on the LED surface penetrating through the LED active layers. This LED will be referred as a *deep etched* LED. The benefit of the deep etched LED is the close proximity of the deposited QDs (acceptors) to the LED active layers (donors) which leads to the increasing of resonant energy transfer rate. A control device with the same hole structures but do not penetrate through the LED active layers is fabricated and referred to as a *shallow etched* LED. Due to the large donor-acceptor separation distance, resonant energy transfer does not occur in the hybrid QD/shallow etched LED. The emission of QD deposited on the deep etched and shallow etched LEDs under the same emission intensity of photons from the QWs are measured in order to observe the effect of resonant energy transfer on the QD emission.

4.1 Streak measurements

Streak cameras are ultra fast tools widely used to investigate temporal evolution of optical phenomena such as photoluminescence decays of materials. By using streak cameras, time-resolved and spectrum-resolved profiles of photoluminescence decays can be measured simultaneously. A schematic diagram of a streak measurement is shown in figure 4.1.

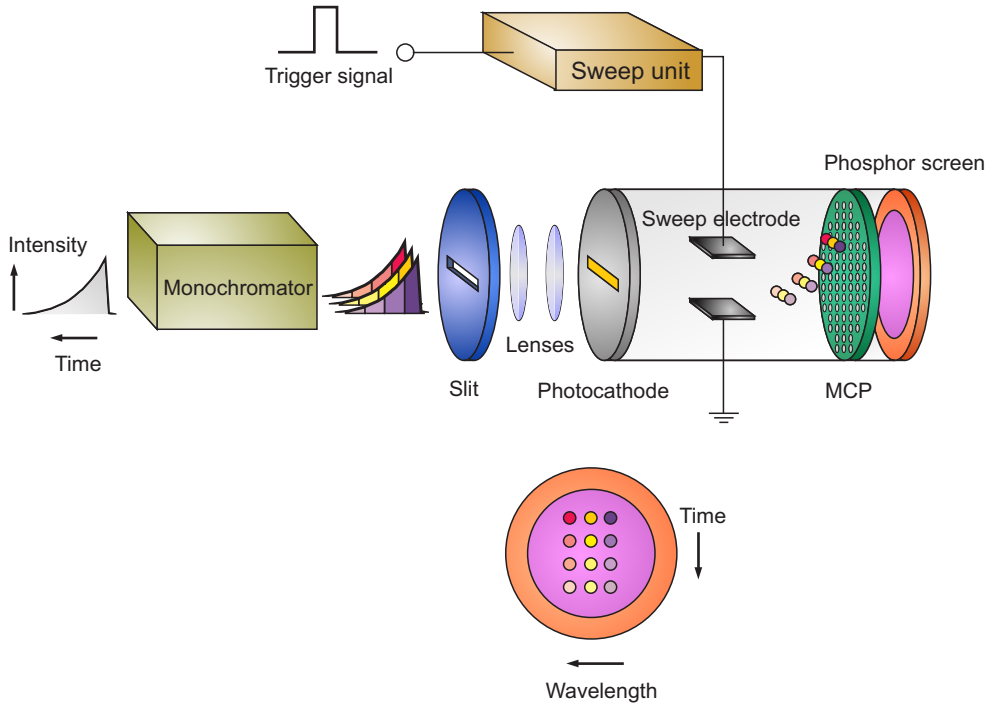

FIGURE 4.1: Schematic diagram of streak measurements

Photoluminescence collected from a sample is passed though a monochromator in order to disperse and select the wavelength of interest. The photoluminescence is subsequently focused on a photocathode by a set of lenses. Photoelectrons are generated as photons strike the photocathode according to the photoelectric effect.

The number of generated photoelectrons is proportional to the intensity of the incident light at each wavelength. The photoelectrons are then accelerated through a pair of sweep electrodes which change the incident angle of the photoelectrons on a micro-channel plate (MCP) and eventually on a phosphor screen. The MCP is an electron multiplier containing a bundle of glass channels with a diameter of about 20 μm. The inner wall of the glass channel is coated with secondary electron emitter materials. A single electron can be multiplied to 10^4 electrons with this MCP. High voltage applied to the sweep electrodes is synchronised with the period of the photons. The electrodes sweep the photoelectrons on the phosphor screen in vertical direction depending on the time they arrive the sweep electrodes. Therefore, time evolution of the photoluminescence can be observed from the vertical spatial evolution on the phosphor screen. Moreover, the spectrum profile of the photoluminescence can be observed simultaneously from the horizontal axis of the phosphor screen. The horizontal and the vertical axes of the phosphor, therefore, represent the spectrum profile and the time evolution of the photoluminescence respectively.

4.2 Materials and methods

Schematic diagrams of deep etched and shallow etched LEDs fabricated by Luxtaltek Corporation are shown in figure 4.2(a) and (b) respectively. A 2 μm thick undoped GaN buffer layer is grown on a sapphire substrate before the deposition of a 2 μm thick n-doped GaN layer. The active layers consisting of 5 periods of undoped InGaN/GaN QWs are grown on the n-doped GaN layer and subsequently a 50 nm thick p-doped AlGaN layer is deposited. The device is terminated by a 0.2 μm thick p-doped GaN layer.

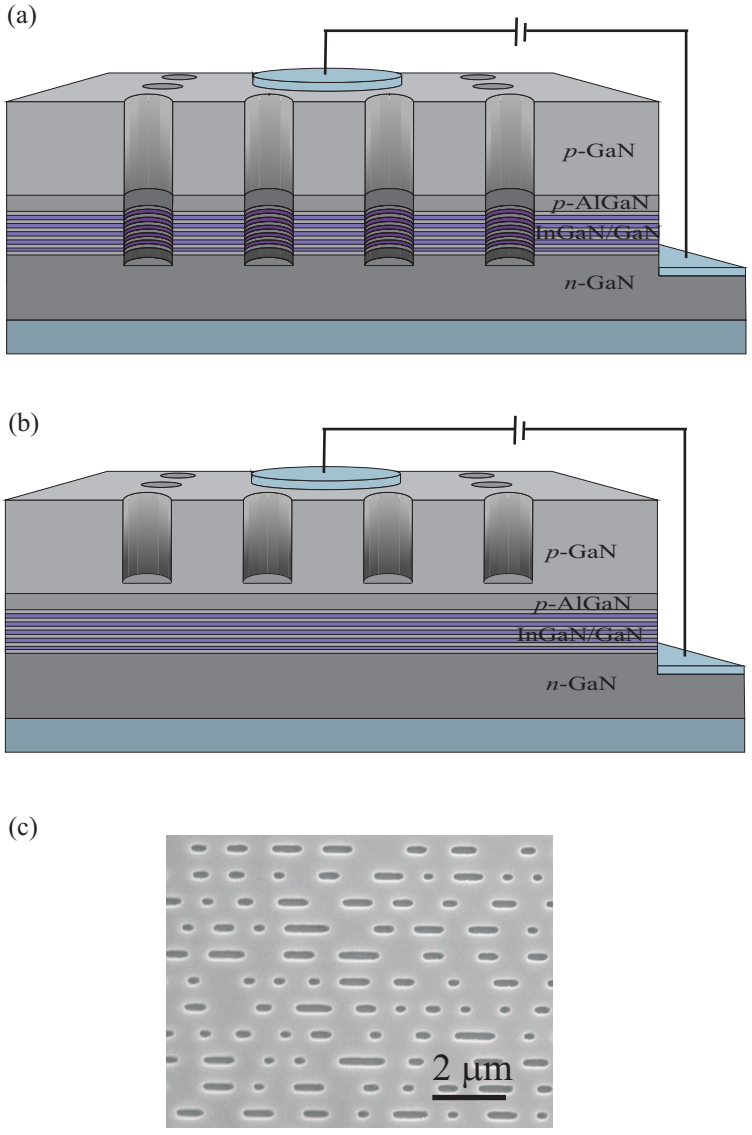

FIGURE 4.2: Schematic diagrams of (a) the deep etched LED. (b) the shallow etched LED. (c) Scanning electron microscope image of the deep etched LED surface.

Nano-imprinting lithography is used to fabricate patterns onto the LEDs. A 50 nm thick SiO_2 layer is initially deposited onto the LEDs by plasma enhanced chemical vapour deposition (PECVD) followed by a spin-coated polymer layer. A mold is brought into contact with the polymer layer under certain pressure. By applying heat above the glass transition temperature of the polymer, the pattern is transferred from the mold to the polymer layer. The LED samples and the mold are then cooled down to room temperature to release the mold. Reactive ion etching (RIE) with CF_4 plasma is used to remove the residual polymer layer and transfer the pattern onto SiO_2.

The patterns of different depths are eventually transferred to the LEDs by using inductively coupled plasma reactive ion etching (ICP-RIE). For deep etched LEDs, 450-nm-deep hole structures with elliptical cross-section are fabricated on the device surface penetrating through the QW layers. In the case of shallow etched LEDs, 150-nm-deep hole structures with the same pattern are fabricated. Cl_2 and Ar etching gases are introduced into the reactor chamber through independent electronic mass flow controllers (MFCs) that can control the flow rate with an accuracy of about 1 sccm. An automatic pressure controller (APC) is placed near the exhaust end of the chamber to control the chamber pressure. The ICP etching rate is determined to be $\sim$7.5 nm/s associated with the conditions: the flow rate ratio Cl_2/Ar=10 sccm/25 sccm with the ICP source power, bias power set at 200 W/200 W and chamber pressure of 2.5 mTorr. The residual SiO_2 layer is subsequently removed by a buffer oxide etchant (BOE). Figure 4.2(c) presents a scanning electron microscope (SEM) image of the hole structures of a deep etched LED.

Highly efficient CdSe/CdS core/shell QDs [98] capped with hexadecylamine,

tri-*n*-octylphosphine oxide (TOPO), and tri-*n*-octylphosphine (TOP) are used as colour-tunable light emitters in the hybrid structure. The hybrid colour-conversion LEDs are prepared by drop casting the QDs onto the LED surface.

The QD and the QW photoluminescence decays at room temperature are measured by a streak camera with 300 ps resolution. The hybrid structures are excited at 400 nm by 100 fs pulses of frequency-doubled output from an amplified Ti:sapphire oscillator. In electroluminescence (EL) measurements, the voltage applied to the heterostructures is controlled by a source-measure unit (Keithley 238) and the electroluminescence is measured by a spectrometer (VS140 Jobin Yvon).

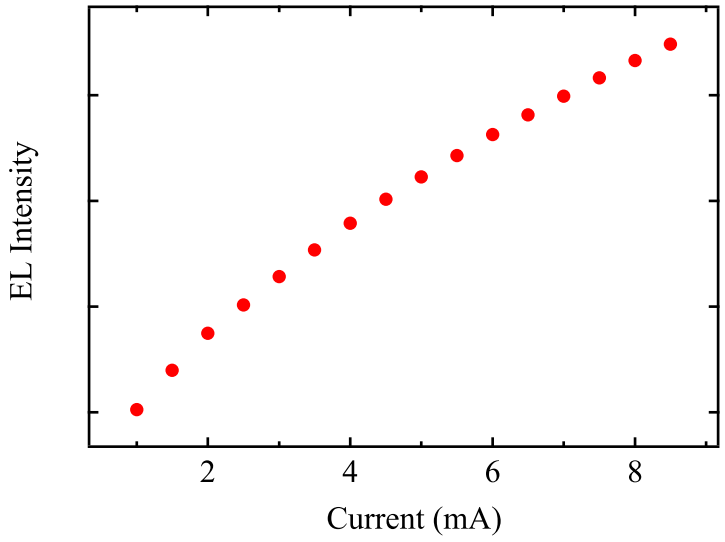

FIGURE 4.3: Electroluminescence intensity of the deep etched LED at different injection current.

4.3 Results and discussions

Spectral overlap of the hybrid QD/deep etched LED structure at room temperature is shown in figure 4.4, where the photoluminescence peaks of the LED and the QDs are at 460 nm and 630 nm respectively. The absorption of the QDs strongly overlaps with the LED emission which satisfies the requirement of resonant energy transfer.

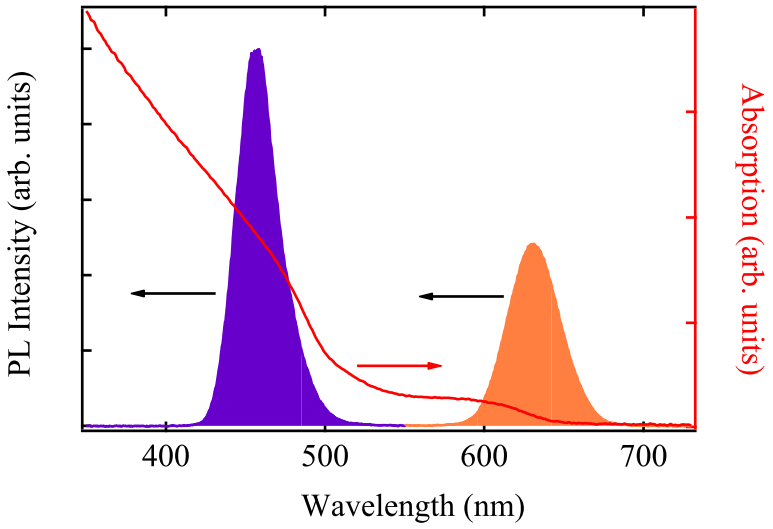

FIGURE 4.4: Spectral overlap of the hybrid QD/deep etched LED structure. The LED (in blue) and the QD photoluminescence (in orange) is at 460 nm and 630 nm respectively. The red solid line is the QD absorption.

4.3.1 Electroluminescence of hybrid colour-conversion LEDs

In figure 4.3, EL intensity of a bare deep etched LED scales linearly with injection current and saturates at high injection current. This result suggests the formation of bound electron-hole pairs or excitons in the active layers of the LED. For deep etched LEDs, surface etching process partly removes the active layers and inevitably introduces surface states to the heterostructures. Consequently, deep etched LEDs

emit less light than shallow etched LEDs (control devices) do at the same injection current. As shown in figure 4.5, the EL intensity of the bare deep etched LED at 7 mA is comparable with that of the bare shallow etched LED at 3.8 mA.

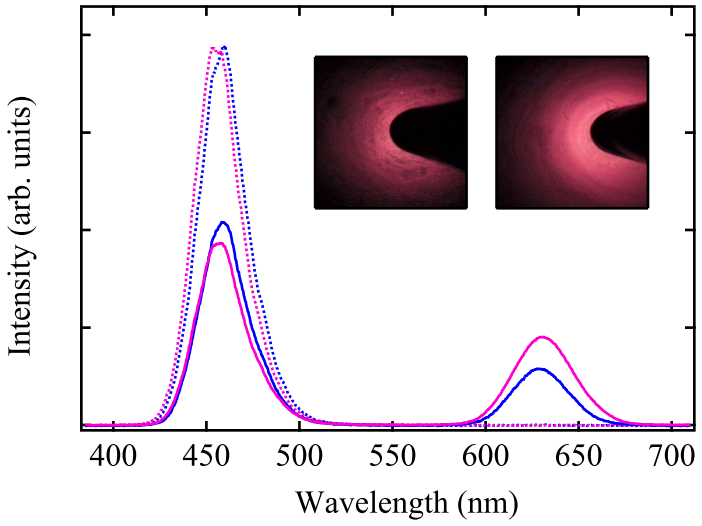

FIGURE 4.5: QW emission of the bare shallow etched LED (blue dotted line) and the bare deep etched LED (pink dotted line) at 3.8 mA and 7 mA respectively. The blue solid line (pink solid line) represents EL of the corresponding hybrid QD/shallow etched LED structure (hybrid QD/deep etched LED structure). Inset: left (right) panel shows the emission of the QDs deposited on the shallow etched (deep etched) LED.

In order to investigate the effect of resonant energy transfer on colour-conversion efficiency, the QD emission pumped by a deep etched LED is compared with the QD emission pumped by a shallow etched LED. For the same EL intensity of the bare LEDs, the QD emission pumped by deep etched LEDs is evidently greater than the QD emission pumped by shallow etched LEDs. Insets of figure 4.5 show the emission of the QDs deposited on a shallow etched LED (left panel) and on a deep etched LED (right panel). Colour-conversion efficiency (η_c) is defined as the ratio of the QD emission intensity in the hybrid structure (I^H_{QD}) to the bare QW emission intensity (I_{QW}), $\eta_c = I^H_{QD}/I_{QW}$ [13]. The average colour-conversion

efficiency of the hybrid QD/deep etched LED in the linear regime is 20%, i.e. 43% increase from that of the hybrid QD/shallow etched LED.

We propose that the enhancement of QD emission in the hybrid QD/deep etched LED structure is due to resonant energy transfer. Charge transfer through the insulating ligands of QDs is inhibited due to the large band-offset between the carriers in the QDs and surface molecules as well as between the QDs and the QWs [99]. Effective resonant energy transfer efficiency (η^*_{ET}) is estimated from $\eta^*_{ET} = 1 - I^H_{QW}/I_{QW}$, where I^H_{QW} is the emission intensity of QW donors in the presence of QD acceptors. Here, η^*_{ET} is averaged over the entire active area including both the area in which carriers undergo resonant energy transfer and the area in which carriers do not. At low injection current, η^*_{ET} decreases as injection current increases and remains constant at higher injection current ($\sim$4 mA) as shown in figure 4.6. It is proposed that the heating and the Coulomb screening at high injection current lead to exciton dissociation and eventually the decrease of η^*_{ET} [100]. Figure 4.6 also shows the average enhancement of the QD emission versus the injection current of the deep etched LED, i.e. the ratio of the QD emission pumped by the deep etched LED to that pumped by the shallow etched LED for an injection current of the latter that produces the same QW emission intensity with the deep etched LED in the bare configuration. Evidently, the enhancement of the QD emission can be observed for all injection current and follows the trend of energy transfer efficiency.

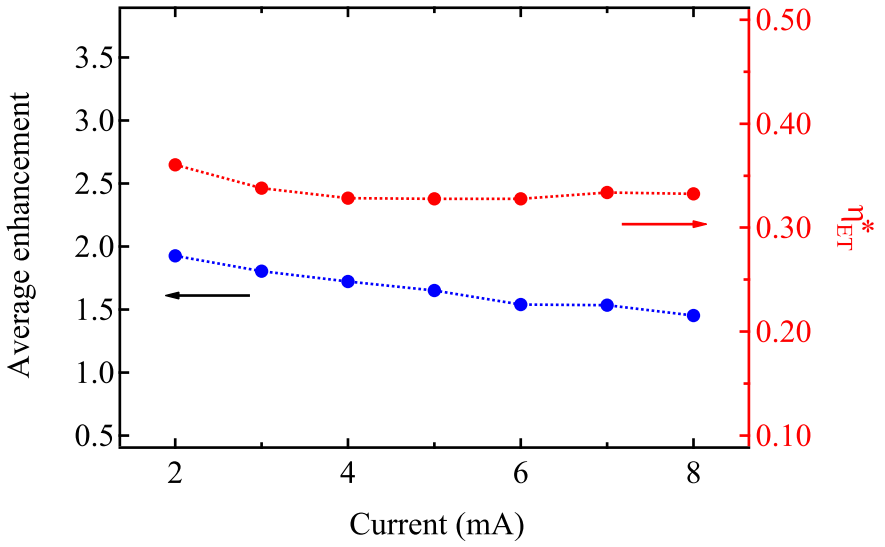

FIGURE 4.6: Effective resonant energy transfer efficiency (red circles) and enhancement of the QD emission (blue circles) at different injection current.

4.3.2 Photoluminescence decay of donors

To verify the existence of resonant energy transfer in the hybrid QD/deep etched LED structure, transient carrier dynamics of the QWs (donors) are investigated. The devices are excited at 400 nm with 100 fs pulses and a 250 kHz repetition rate. Photoluminescence decays of the shallow etched and the deep etched LEDs at room temperature are illustrated in figure 4.7(a) and 4.7(b) respectively. Figure 4.7(c) shows a streak image and the energy window used to extract the QW photoluminescence decay. The QW photoluminescence decays of the shallow etched LED with and without the deposited QDs are virtually identical. These results suggest that resonant energy transfer does not occur in the QD/shallow etched LED structure due to the large donor-acceptor separation distance (∼100 nm). Hence, the QD emission is solely the effect of conventional radiative energy transfer. In contrast, the QW photoluminescence decay of the deep etched LED changes after the QD

deposition as shown in figure 4.7(b). The QW photoluminescence with deposited QDs decays faster during the first 4 ns and slower at later time compared to the bare QW. The faster decay is attributed to an additional decay channel due to resonant energy transfer. The slower decay at later time ($t > 8$ ns) is considered to be the effect of surface passivation of the etched QW from the organic ligands of the deposited QDs ($k_{QW} = 0.15$ ns^{-1}, k_{QW}^{H}=0.12 ns^{-1}).

Since resonant energy transfer decreases dramatically with increasing donor-acceptor separation distance, not all electron-hole pairs in the QWs undergo resonant energy transfer. Hence, the electron-hole pairs are categorised into two groups, i.e. the ones contribute to resonant energy transfer and the ones do not. The QW photoluminescence decay can be approximated with an exponential decay for the first 4 ns as shown in the inset of figure 4.7(b). To extract the actual resonant energy transfer rate (k_{ET}) and the percentage of electron-hole pairs that undergo resonant energy transfer, the QW photoluminescence decay with the deposited QDs is fitted with the following equation,

$$I_{QW}^{H}(t) = Ae^{-k_{QW}t} + Be^{-(k_{QW}+k_{ET})t}, \tag{4.1}$$

where A and B are fractions of the electron-hole pairs that do not undergo and undergo resonant energy transfer respectively and $k_{QW} = 0.18$ ns^{-1} is the total decay rate of the etched QWs taking into account the effect of surface passivation. From the fit, $k_{ET} = 0.81 \pm 0.02$ is obtained corresponding to the energy transfer efficiency of $82 \pm 3\%$ and the number of the electron-hole pairs that experience resonant energy transfer is estimated to be $18 \pm 0.1\%$. The transfer efficiency of 65% was recently reported for a hybrid structure produced by drop casting colloidal

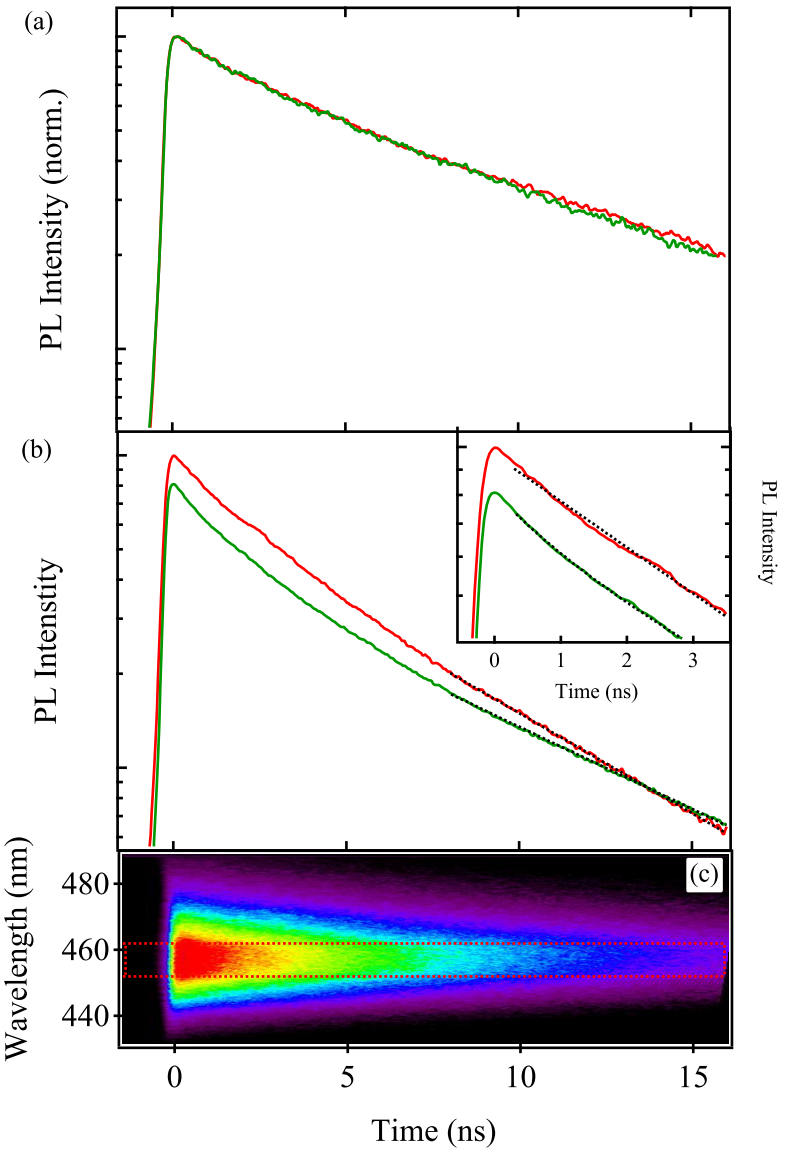

FIGURE 4.7: (a) QW photoluminescence decay of the shallow etched LED with (green solid line) and without (red solid line) deposited QDs. (b) QW emission decay of the deep etched LED with (green solid line) and without (red solid line) deposited QDs. Dotted lines are fittings described in text. Inset shows the effect of resonant energy transfer on the QW photoluminescence decay during early decay period. (c) Streak image of the QW photoluminescence decay and the window (red dashed line) used to extract the QW photoluminescence decay.

QDs onto a single InGaN/GaN QW with a 2 nm capping layer [6]. Here, the close proximity of the QDs to the QWs due to the patterned structures improves the transfer efficiency.

From an SEM image of the LED surface in figure 4.2, ∼3% of the electron-hole pairs created in the active area would undergo energy transfer in static situation assuming resonant energy transfer occurs within 10 nm from the etched interface. However, diffusion of the electron-hole pairs towards the etched interface should be taken into account in the transfer process. A two-dimensional Monte Carlo simulation is established to explore carrier dynamics in this system including carrier diffusion effects. In this model, the motion of electron-hole pairs in the active layer is governed by thermal energy and the scattering with impurities or phonons is described by scattering time (τ_s). The QW decay rate (k_{QW}) and the energy transfer rate (k_{ET}) are obtained from the experiments above. The scattering time of carriers in InGaN QWs is estimated from $\tau_s = m^*\mu/e$, where m^* is the effective mass, and μ is the carrier mobility. The carrier mobility of InGaN/GaN quantum wells varies in the literature [101, 102] leading to a broad value of the scattering time. Nevertheless, for the scattering time in the range of 0.001 ps to 1 ps in the simulation, 18% of the electron-hole pairs in the active layer undergo resonant energy transfer. The results from the simulation are in good agreement with the fit of the experimental results.

Figure 4.8 shows the percentage of excitons in the QW that experience resonant energy transfer for different energy transfer length. The energy transfer length is defined as the average distance from the QW/air interface where excitons within this length can undergo resonant energy transfer. The fit in figure 4.7(b)

suggests that ∼18% of the excitons in the active layer undergo resonant energy transfer which corresponds to the simulation result of 10 nm energy transfer length.

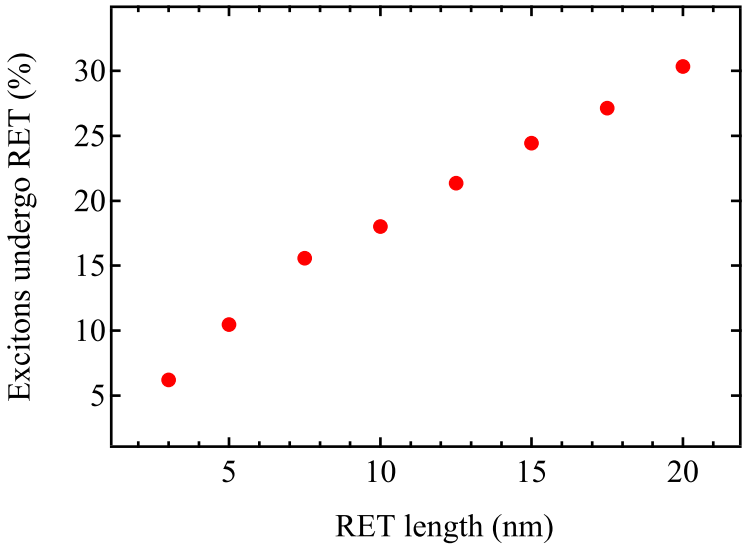

FIGURE 4.8: Percentage of excitons that undergo resonant energy transfer for different energy transfer lengths.

4.3.3 Photoluminescence decay of acceptors

The existence of resonant energy transfer in the hybrid QD/deep etched LED structure is demonstrated at the donor site by the faster photoluminescence decay of the QW in the presence of the deposited QDs. Also the transient carrier dynamics of the QDs (acceptors) are explored in order to have the conclusive demonstration. Figure 4.9(a) and 4.9(b) show the photoluminescence decay of the QDs deposited on the deep etched and shallow etched LEDs respectively. Obviously, the photoluminescence intensity of the former is greater than the latter suggesting the occurrence of resonant energy transfer in the hybrid QD/deep etched LED.

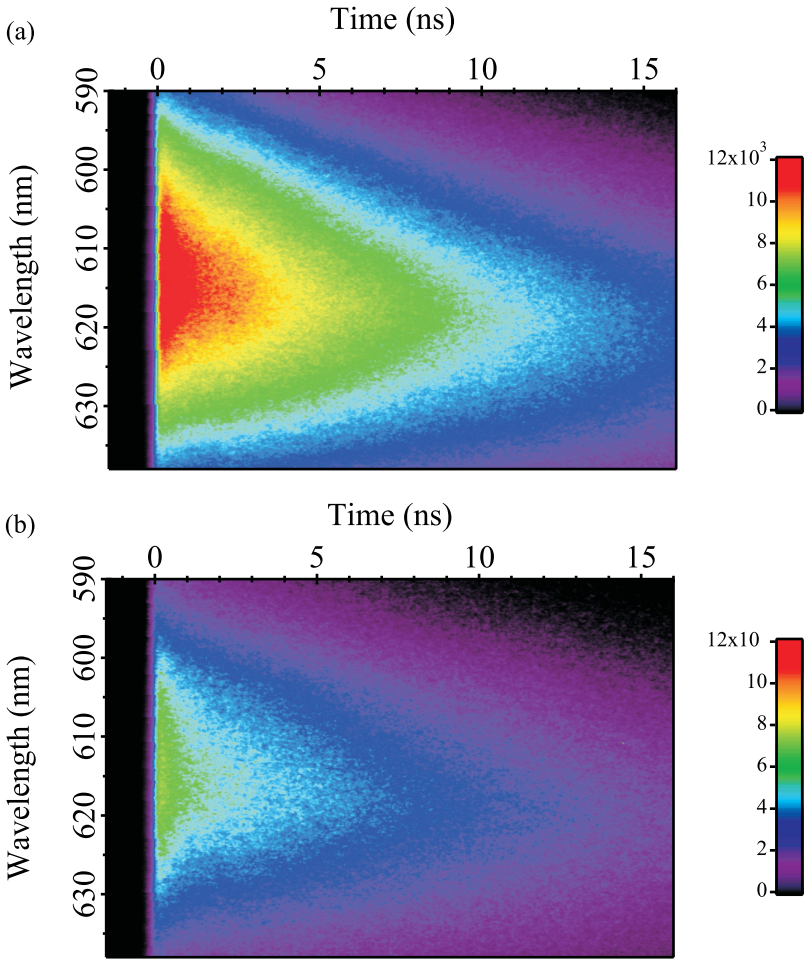

FIGURE 4.9: Fluorescence decays of the QDs deposited on (a) deep etched LED (b) shallow etched LED.

The normalised data of figure 4.9(a) is subtracted by those of figure 4.9(b) and presented in figure 4.10(a). The additional carrier injection from the QWs to the QDs via resonant energy transfer is presented by the blue area. A 20-nm window centred at the QD emission peak, indicated by the green dashed line in figure 4.10(a), is used to extract the average transient carrier dynamics of the QDs. The peak in figure 4.10(b) suggests carrier injection from the QWs to the QDs.

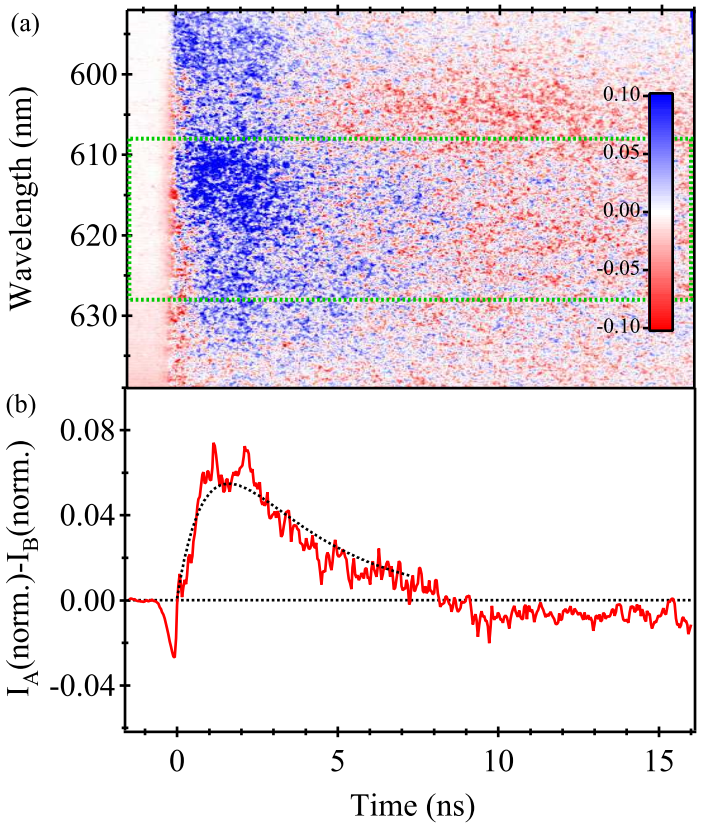

FIGURE 4.10: (a) Difference of transient fluorescence dynamics calculated from the normalised data of figure 4.9(a) and 4.9(b). (b) The average difference of transient fluorescence dynamics extracted from a 20 nm window centered at the peak of QD emission. Dotted line is the fitting described in text.

The transient carrier dynamics of the QDs deposited on the deep etched LED is given by the following equation [8],

$$I_{QD}^{H}(t) \propto \frac{k_{ET}}{k_{QD} - k_{QW} - k_{ET}} \left(e^{-(k_{QW}+k_{ET})t} - e^{-k_{QD}t} \right), \tag{4.2}$$

where k_{QD} is the QD photoluminescence decay rate. By using the parameters obtained from above experiments in table 4.1, the transient carrier dynamics can be fitted by the above equation verifying the occurrence of resonant energy transfer

in the hybrid structure.

Parameter	Value (ns^{-1})
k_{QW}	0.18
k_{QD}	0.35
k_{ET}	0.81

TABLE 4.1: Parameters used in the fit of the QD photoluminescence decay in the hybrid structure.

4.4 Conclusions

A novel colour-conversion LED consisting of a surface-patterned blue LED and colloidal QDs offers a route to overcome the low carrier transfer of colloidal QDs. Electrically injected carriers in the blue emitter are efficiently transferred to the adjacent QDs via resonant energy transfer in addition to conventional radiative energy transfer. As a result, a twofold enhancement of the QD emission is achieved.

The existence of resonant energy transfer in the hybrid QD/deep etched LED structures is verified by exploring transient carrier dynamics of the QWs and the QDs. The increase of the QW photoluminescence decay rate is an indication of resonant energy transfer. Moreover, the comparison of photoluminescence decays of the QDs deposited on the shallow and deep etched LEDs suggests carrier injection from the deep etched LED to the QDs via resonant energy transfer.

Chapter 5

Photocurrent Enhancement in Hybrid Light Harvesting Devices

Despite the outstanding optical properties of colloidal QDs, the efficiency of QD-based PV cells has not exceeded that of Si-based PV cells. An inherent drawback of colloidal QDs leading to the low efficiency is known as their low carrier transfer. In section 5.2, hybrid QD/patterned QW structures are designed and fabricated to use in light harvesting applications. In the hybrid structure, highly absorbing QDs absorb photons and transfer the excitation energy to a high-mobility patterned QW via resonant energy transfer. Patterned structures are designed to bring the colloidal QDs into close proximity with the QWs which leads to the enhancement of energy transfer rate. Electron-hole pairs in the patterned QW are subsequently separated by the built-in electric field and collected by the corresponding electrodes.

The investigated hybrid configuration releases potential of using colloidal QDs as highly efficient absorbers in light harvesting devices, while overcoming their low carrier transfer efficiency.

In section 5.3, the patterned QW heterostructure is replaced by a patterned bulk heterostructure. The semiconductor bulk heterostructure offers higher carrier transport efficiency than the QW heterostructure and leads to high performance devices.

5.1 Nanostructuring by focused ion beam

A focused ion beam (FIB) is a high resolution tool widely used in various fabrication areas such as circuit modification, sample preparation for transmission electron microscopy (TEM) and nanostructure deposition. The operating principle of the FIB is similar to that of the scanning electron microscope (SEM). While an electron beam is used in the SEM, a focused beam of ions such as Ga^+ is used in the FIB. A schematic diagram of an FIB system is shown in figure 5.1. The Ga^+ ions created from a liquid metal ion source (LMIS) by application of high electric field are accelerated to energy of 10-50 keV and collimated by the first electrostatic lens. Astigmatism of the beam is corrected by the upper octupole. The beam current and the resolution are adjusted by changing the size of a selectable aperture. High current beam is suitable for a rough and fast milling whereas low current beam is used when high resolution is required. The beam can be blanked by the blanking plates placed after the aperture. The Ga^+ beam is precisely controlled by the lower octupole and is focused onto the sample by the second electrostatic lens.

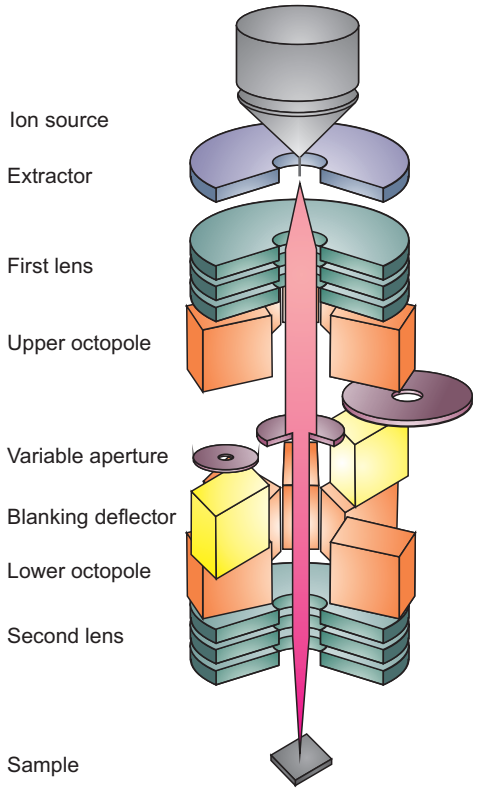

FIGURE 5.1: Schematic diagram of a focused ion beam

As the energetic ions hit the sample, secondary particles such as neutral atoms, ions and electrons are created. In the imaging mode, the ions or the electrons are collected by biased detectors. Positively biased detectors are used to collect secondary electrons whereas negatively biased detectors are used to collect secondary ions. In the machining mode, the ion beam is scanned over the sample with longer dwell time to make designed patterns.

5.2 Photocurrent enhancement in hybrid QD/patterned QW heterostructures

5.2.1 Materials and methods

Figure 5.2(a) presents a schematic diagram of a heterostructure fabricated at University of Nottingham. The heterostructure is grown by molecular beam epitaxy (MBE) on a (100) GaAs substrate and fabricated into *p*-*i*-*n* devices of 400 μm diameter. A 1 μm thick layer of *n*-doped GaAs is grown on the GaAs substrate followed by a 100 nm thick layer of undoped $Al_{0.4}Ga_{0.6}As$. Undoped multiple QW layer is subsequently grown before the deposition of a 100 nm thick layer of undoped $Al_{0.4}Ga_{0.6}As$ and a 500 nm thick layer of *p*-doped $Al_{0.4}Ga_{0.6}As$. The active layer contains 20 periods of 7.5 nm thick GaAs wells and 12 nm thick $Al_{0.4}Ga_{0.6}As$ barriers. The heterostructure is finalised by a 250 nm thick layer of *p*-doped GaAs. The top contact of the structure is an open circular mesa. The energy band of the heterostructure is shown in figure 5.2(b).

In figure 5.3(a), an 80×80 μm^2 array of rectangular channels is fabricated on the top surface of the heterostructure penetrating through the QW layers by using focused Ga^+ ion beam (FIB). The channels are 570 nm wide and 1.4 μm deep and separated by 1.5 μm wide rectangular bars as shown in the top inset of figure 5.3(a). Colloidal CdSe/CdS core/shell QDs are synthesised by an organometallic method [98]. The QDs are capped with hexadecylamine, tri-*n*-octylphosphine oxide (TOPO), and tri-*n*-octylphosphine (TOP) and eventually dissolved in chloroform. The hybrid structure is fabricated by drop casting the colloidal QDs on the patterned heterostructure. The bottom inset of figure 5.3(a) shows an SEM image of the

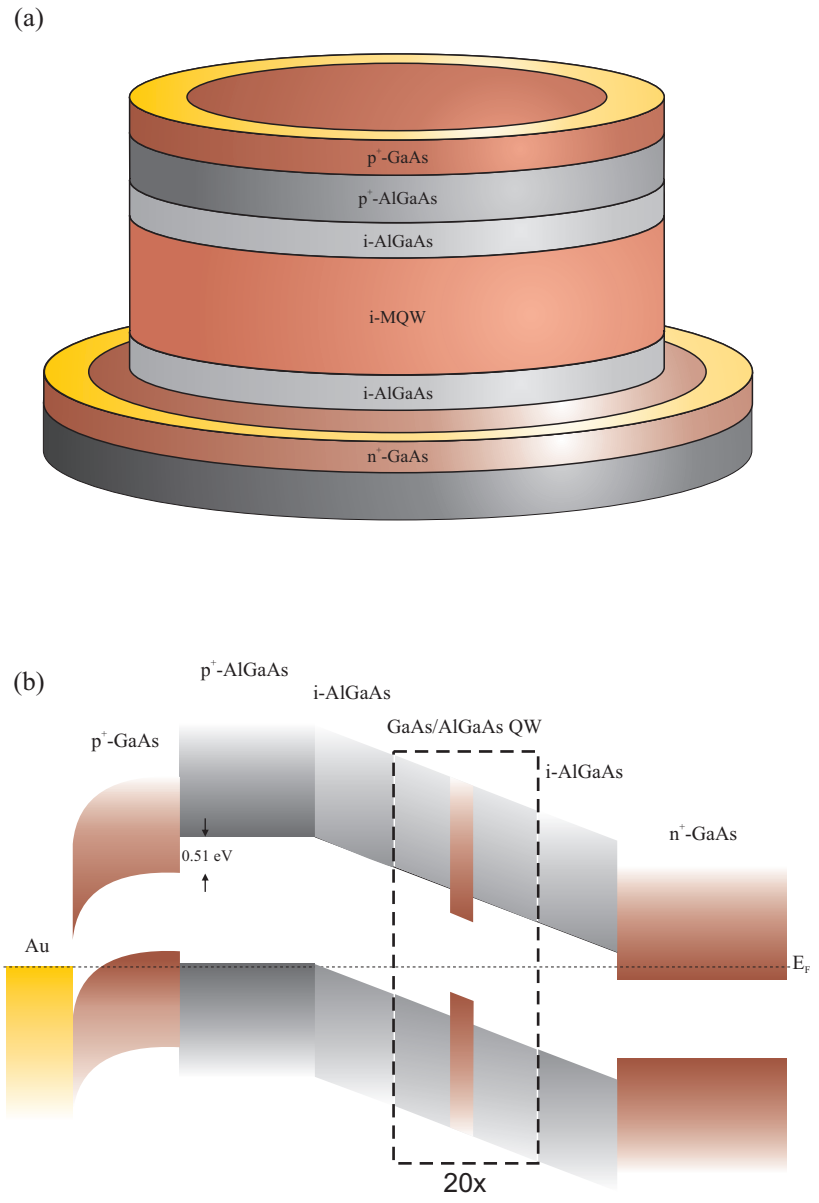

FIGURE 5.2: (a) Schematic diagram of the semiconductor heterostructure. The heterostructure consists of 20 periods of 7.5 nm thick GaAs wells with 12 nm thick AlGaAs barriers. (b) Energy band of the heterostructure

patterned heterostructure after the QD deposition. A control device is constructed by depositing the colloidal QDs on the top surface of a flat heterostructure.

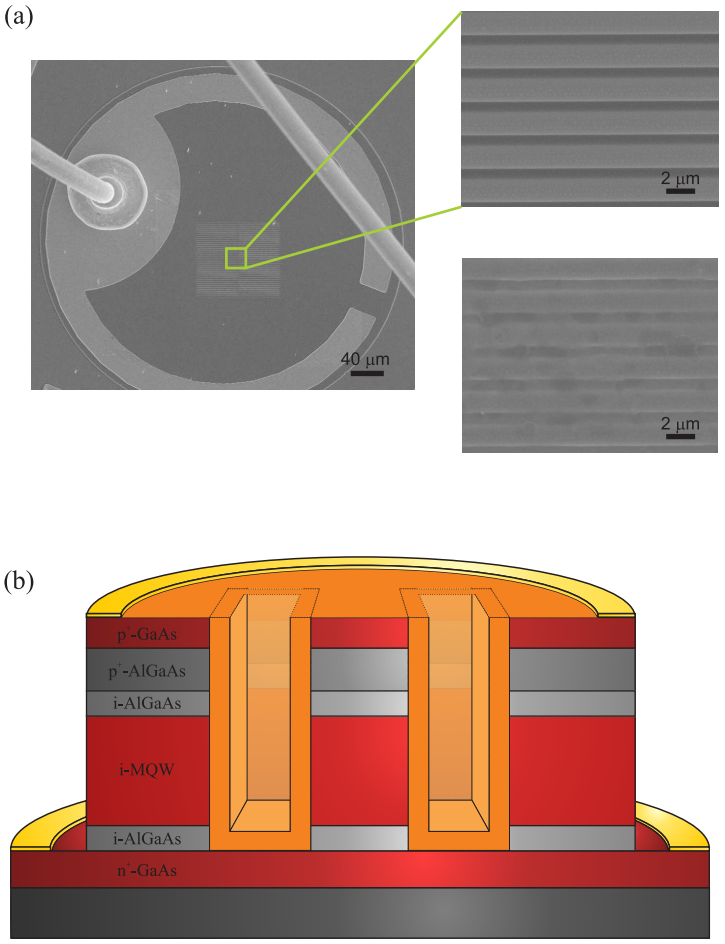

FIGURE 5.3: (a) Scanning electron microscope (SEM) images of the patterned heterostructure. The top and the bottm right insets are the magnified images of the channels before and after the QD deposition respectively. (b) Schematic of the hybrid patterned device where the channels are partially filled with the QDs.

To measure photoluminescence decays of the heterostructures and the colloidal QDs, time-correlated single photon counting (TCSPC) technique with 40 ps resolution is used together with a monochromator and additional optical filters to spectrally resolve the spectra. The heterostructure is installed in a sample holder

which has electrical contacts to connect the *p-i-n* heterostructure and the photocurrent measurement units. The sample holder is attached to a cold finger in a close cryostat in which the temperature can be varied from 25 K to room temperature.

5.2.2 Results and discussions

Figure 5.4 shows the emission and the absorption of the QDs. The emission peak is ∼610 nm at 25 K. Photocurrent of the heterostructure illustrates the heavy hole and light hole peaks together with the peak of the AlGaAs topmost barrier (∼585 nm). The QW emission (∼780 nm) is also shown in figure 5.4. The QDs are deliberately chosen to have the emission energy slightly less than the energy gap of AlGaAs in order to create energetic carriers in the heterostructure. The possibility of the energetic carriers to escape the QWs is greater than the low energy carriers. Therefore, relatively high carrier extraction is expected by using these QDs.

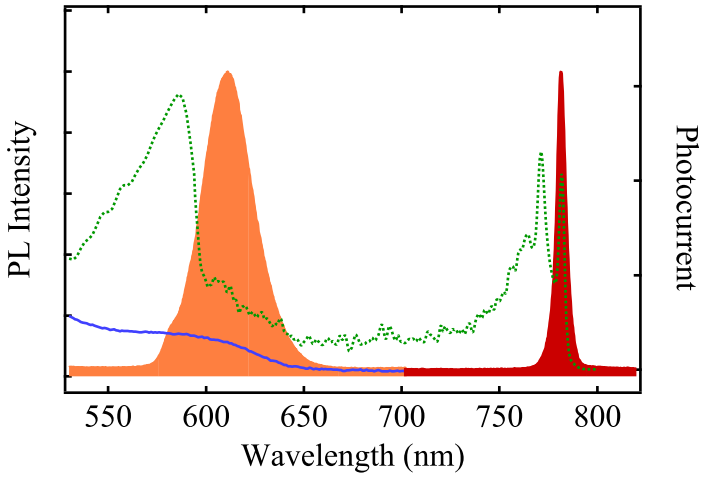

FIGURE 5.4: Spectral overlap of the hybrid structure. The QD fluorescence is in orange and the blue solid line is the QD absorption. The green dotted line is the photocurrent of the heterostructure at 25 K. The QW photoluminescence is illustrated in red.

During the patterning process, surface states are inevitably introduced to the heterostructures, specifically at the channel facets. The surface states are known to trap the QW carriers resulting in the increase of nonradiative recombination rate. Consequently, as shown in figure 5.5 the total QW decay rate, $k_{tot} = k_{rad} + k_{non}$, increases where k_{rad} and k_{non} are radiative and nonradiative decay rates respectively. Surface states become crucial as the dimensionality of materials decreases, particularly in colloidal QDs, due to the increase of the ratio between surface atoms and bulk atoms. It has been reported that the surface states of colloidal QDs can be passivated by organic capping layers such as tri-n-octylphosphine oxide (TOPO) and tri-n-octylphosphine (TOP). Recently colloidal QDs with quantum yield reaching 100% were successfully achieved [103].

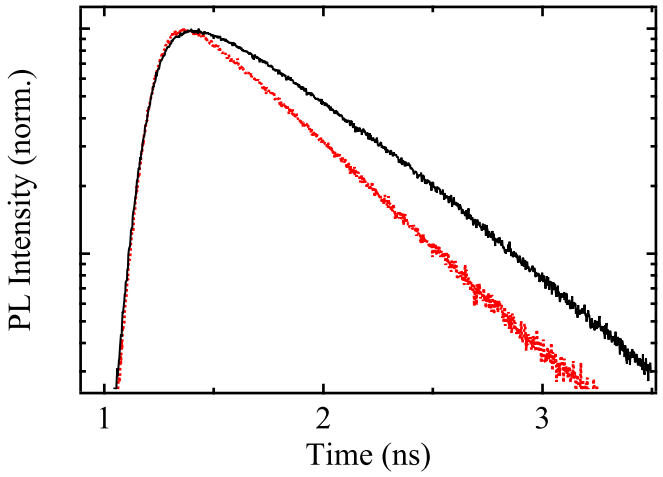

FIGURE 5.5: QW photoluminescence decays of the flat (solid black line) and patterned (solid red line) heterostructure at 25 K.

5.2.2.1 Photoluminescence decay of donors

To verify the existence of resonant energy transfer in the hybrid patterned structure, photoluminescence decay of the colloidal QDs (donors) deposited on the patterned

heterostructure is measured by using TCSPC technique with 400 nm excitation wavelength and compared with photoluminescence decay of the QDs deposited on a glass substrate at 25 K as shown in figure 5.6(a). The photoluminescence decay rate of the former is evidently higher than that of the latter. The faster decay indicates an additional decay channel from the QDs to the QWs via resonant energy transfer. Hence, the QD photoluminescence decay rate in the hybrid structure (k_{QD}^{H}) is given by $k_{QD}^{H} = k_{QD} + k_{ET}$, where k_{QD} and k_{ET} are QD photoluminescence decay rate and resonant energy transfer rate respectively.

In order to estimate the resonant energy transfer efficiency in the hybrid structures, a carrier dynamics model is established. Since resonant energy transfer is proportional to the donor-acceptor separation distance, only the QDs close to the channel facets experience resonant energy transfer. Therefore, the QDs deposited on the patterned heterostructure are categorised into two groups, the QDs that experience resonant energy transfer and the ones that do not. The photoluminescence decay of the QDs deposited on a glass substrate can be described by biexponential decay. The photoluminescence decay of the QDs deposited on the patterned heterostructure can be described by:

$$I(t) = \sum_{i=1,2} A_i \cdot e^{-k_{QDi}^{H} t} + \sum_{i=1,2} B_i \cdot e^{-k_{QDi} t}, \tag{5.1}$$

where $i = 1$ and 2 define the fast and slow components respectively. The first two terms correspond to the photoluminescence decay of the QDs that undergo energy transfer and the other terms correspond to the photoluminescence decay of the QDs that do not contribute to the energy transfer. Figure 5.6(b) shows the photoluminescence decay of the QDs deposited on a glass substrate compared

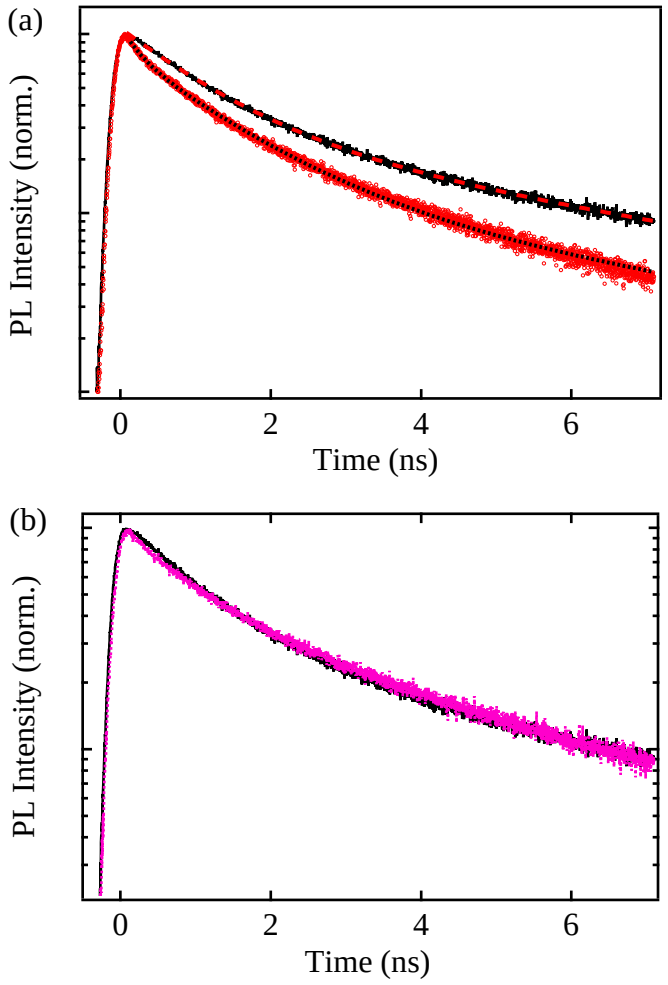

FIGURE 5.6: (a) Fluorescence decays of the QDs deposited on a glass substrate (black solid line) and on the patterned heterostructure (red open circles). The red dashed and the black dotted lines are fitting curves of the QD fluorescence on a glass substrate and on the patterned heterostructure respectively. (b) Fluorescence decay of the QD deposited on a glass substrate (black solid line) and on the flat heterostructure (pink solid line).

to that of the QDs deposited on a flat heterostructure. The decays are virtually identical suggesting the interdot energy transfer of the QDs on both materials can be estimated to be the same. Since the energy transfer rate scales linearly with quantum yield of the donors, i.e. the QDs, the relationship between the energy transfer rate and the QD photoluminescence decay rate is given by $\frac{k_{ET1}}{k_{ET2}} = \frac{k_{QD1}}{k_{QD2}}$. By fitting the photoluminescence decay of the QDs deposited on the patterned

heterostructure with equation 5.1 ($k_{QD1} = 0.9$ ns^{-1} and $k_{QD2} = 0.2$ ns^{-1}), the energy transfer efficiency of 79% is obtained. The high transfer efficiency in this work is explained by the close proximity of the donors and acceptors. The QDs that experience resonant energy transfer is estimated from the fitting to be ∼80% suggesting a thin layer of the QDs is deposited on the patterned structure.

5.2.2.2 Photoluminescence decay of acceptors

QW photoluminescence decays are measured in order to further investigate carrier dynamics in the hybrid structures. The heterostructures are excited at 584 nm and a monochromator together with appropriate optical filters is used to spectrally resolve the QW photoluminescence. Photoluminescence decays of the patterned heterostructure with and without colloidal QD deposition are shown in figure 5.7(a). Evidently, the rise time of the patterned QW emission is longer in the presence of the QDs. The extended rise time can be attributed to carrier injection from the QDs to the QWs via resonant energy transfer. Another important point of these measurements is the alteration of the QW photoluminescence decay at later time ($t > 1$ ns). The photoluminescence decay rate of the hybrid patterned heterostructure (k^H_{QW}) is 16% slower than that of the bare patterned structure (k_{QW}), $k_{QW} = 2.13$ ns^{-1} and $k^H_{QW} = 1.78$ ns^{-1}. The slower decay rate at later time is attributed to the passivation of the surface states in the patterned heterostructure by the organic ligands of the colloidal QDs used here. The comparison of the late photoluminescence decay of the hybrid patterned heterostructure and the flat heterostructure is shown in figure 5.7(b). The decays are virtually identical within ∼1% variation suggesting that the QDs passivate the surface states in the patterned heterostructure and eliminate the nonradiative recombination centres introduced in the patterning

process. Although the nature of the passivation is not fully understood, the carrier dynamics in the QW suggest the elimination of the nonradiative recombination centres.

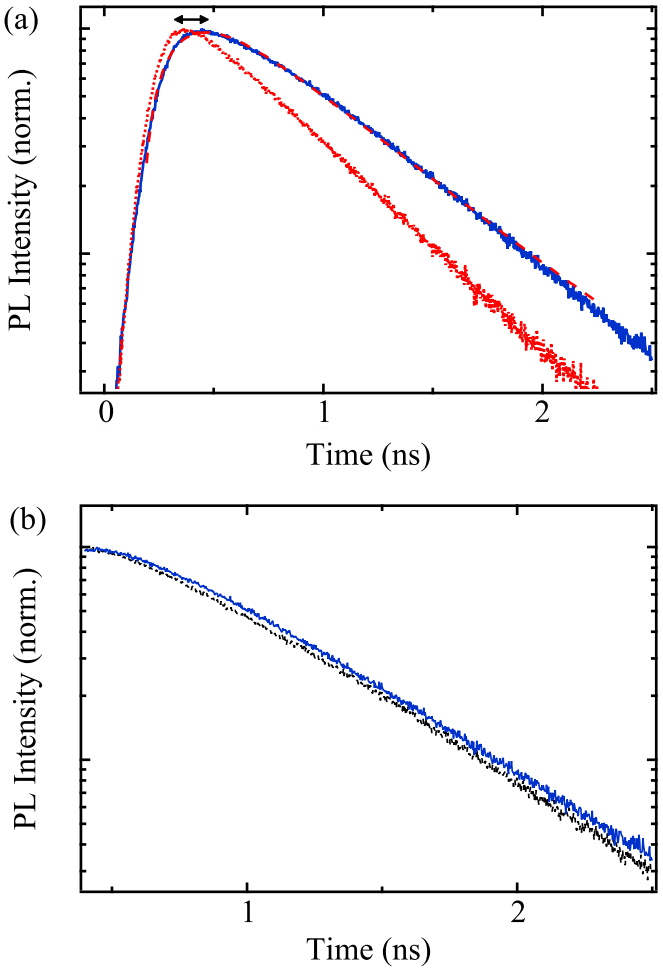

FIGURE 5.7: (a) QW photoluminescence decay of the bare patterned heterostructure (solid red line) and the hybrid patterned structure (solid blue line) at 25 K. The red dashed line presents the fitting given by equation 5.4. (b) QW photoluminescence decay of the hybrid patterned structure (solid blue line) and the flat heterostructure (black solid line) at 25 K.

Carrier dynamics in the hybrid structure can be described by the following set of equations:

$$\frac{dN_{QDi}}{dt} = -k_{QDi}N_{QDi} - k_{ETi}N_{QDi}, \tag{5.2}$$

$$\frac{dN_{QW}}{dt} = -k_{QW}N_{QW} + \sum_i k_{ETi}N_{QDi} + f(t), \tag{5.3}$$

where $f(t)$ is the direct optical pumping. These equations can be solved analytically and the QW photoluminescence decay in the presence of deposited QDs is given by:

$$I(t) = \sum_{i=1,2} \frac{N_{QDi}(0)k_{ETi}}{k_{QW} - k_{QDi} - k_{ETi}} \left(e^{-(k_{QDi}+k_{ETi})t} - e^{-k_{QW}t}\right) + f(t), \tag{5.4}$$

where $N_{QDi}(0)$ is the initial population of the deposited QDs. In figure 5.7(a), the experimental photoluminescence decay of the QW in the hybrid structure can be described by this analytical solution where the fitting parameters presented in table 5.1 are obtained from the above measurements.

Parameter	Value (ns^{-1})
k_{QW}	2.1
k_{QD1}	0.9
k_{QD2}	0.2
k_{ET1}	3.5
k_{ET2}	0.6

TABLE 5.1: Parameters used in the fit of the QD photoluminescence decay in the hybrid structure.

5.2.2.3 Photocurrent enhancement

The benefit of resonant energy transfer in the hybrid patterned structure is revealed by comparing photocurrent of the hybrid patterned and the hybrid flat structures. The heterostructures are excited at 400 nm with 100 fs excitation pulses of a 250 kHz repetition rate by an optical parametric amplifier (OPA). The excitation wavelength is chosen to minimise the effect of the direct excitation on the photocurrent. The laser beam is focused to a spot size (∼40 μm) smaller than the pattern in the heterostructure. Photocurrent of the flat heterostructure is mainly generated from the traditional radiative energy transfer since the separation distance between the QD layer and the QWs is large (∼850 nm) resulting in no contribution of resonant energy transfer to the photocurrent. In contrast, resonant energy transfer is expected to affect photocurrent of the hybrid patterned structure considering photoluminescence data of the QDs and the QWs in the previous sections. As shown in figure 5.8, photocurrent of the hybrid patterned structure is evidently higher than that of the hybrid flat structure.

Photocurrent (I) of the hybrid flat structure scales linearly with the pump fluence (P), $I \propto a_c P$, where a_c is power conversion constant. Whereas photoluminescence intensity of the QDs deposited on a glass substrate demonstrates linear behaviour with the pump fluence as shown in the inset of figure 5.8, the photocurrent of the hybrid patterned structure shows saturation behaviour for the pump fluence higher than 60 μJ/cm^2. The photocurrent saturation here is attributed to the non-linearity of the QWs such as non-linear absorption [104, 105]. Photocurrent of the hybrid patterned structure can be described by $I = I_s\left(1 - e^{-a_H P}\right)$, where I_s and $a_H^{-1} = 76.9$ μJ/cm^2 are the saturation photocurrent and the threshold

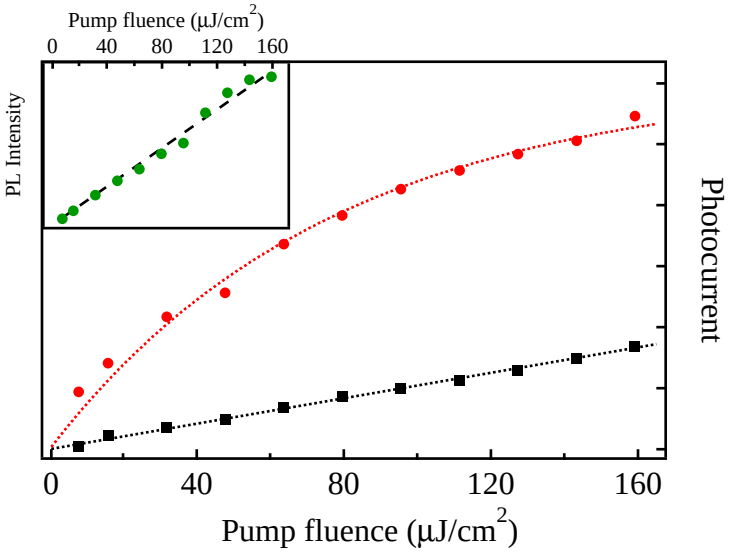

FIGURE 5.8: Pump fluence dependence of the photocurrent of the hybrid patterned (red circles) and the flat-control structure (black squares). The inset shows the pump fluence dependence of the QD fluorescence intensity.

power respectively. For linear regime of the photocurrent, the enhancement of the photocurrent conversion efficiency is given by $(I_s \cdot a_H)/a_c = 6$. The existence of resonant energy transfer in the hybrid patterned structure obviously improves the photocurrent conversion efficiency.

The contribution of resonant energy transfer and conventional radiative energy transfer to photocurrent of the patterned heterostructure can be estimated from $\frac{k_{ET}}{k_{QD} \cdot Q_{QD}}$, where Q_{QD} is the quantum yield of the QDs. By using the parameters obtained from the experiments and $QY_{QD} \approx 40\%$ for the QD used here, the contribution of the resonant energy transfer is ~10 times higher than that of the conventional radiative energy transfer.

5.2.3 Summary

A hybrid structure consisting of colloidal QDs and a patterned QW heterostructure is designed and fabricated to use in light harvesting applications. By engineering the QD emission and the heterostructure absorption, photogenerated excitations in the QDs can be transferred to the heterostructure via resonant energy transfer. The close proximity of the QDs to the active layers of the patterned heterostructure offers efficient resonant energy transfer. Photoluminescence decays of the QWs and the QDs demonstrate the conclusive evidence of resonant energy transfer in the hybrid patterned structures. Consequently, a sixfold enhancement of the photocurrent conversion efficiency is achieved.

5.3 Photocurrent enhancement in hybrid QD/patterned bulk heterostructures

5.3.1 Materials and methods

Figure 5.9(a) presents a schematic diagram of a semiconductor heterostructure fabricated at University of Nottingham. The heterostructure is grown by molecular beam epitaxy (MBE) on a (100) GaAs substrate. A 2.3 μm thick layer of n-doped GaAs is grown on the substrate followed by a 1 μm thick undoped-GaAs layer and a successive 500 nm thick p-doped GaAs layer. A 43 nm thick layer of p-doped $Al_{0.4}Ga_{0.6}As$ layer is subsequently grown before the top layer of 220 nm thick p-doped GaAs. The heterostructure is fabricated into circular mesas of 400 μm diameter with the top metal contact attached to the p-doped GaAs layer and

the second contact attached to the n-doped GaAs layer. Figure 5.9(b) illustrates SEM images of the patterned heterostructure. Channels of 300 nm wide and 1.8 μm deep separated by 1.9 μm wide bars are fabricated on the p-i-n heterostructure by a focused Ga^+ ion beam (FIB). Water soluble CdTe QDs capped with mercapto-propionic acid (MPA) are prepared by aqueous synthesis method [106]. The hybrid patterned device is prepared by drop casting the QDs on the patterned heterostructure. The QDs are also deposited on an unpatterned heterostructure to use as a control reference.

Current-voltage characteristics of the hybrid structure is measured by using a Keithley 238 source-measure unit (SMU). A HP-VEE program is written to control the SMU for current-voltage measurements and save data to a computer.

5.3.2 Results and discussions

As the active layer of the heterostructure is partly removed to fabricate the channels, surface states are inevitably introduced to the heterostructure in the patterning process. The surface states serve as recombination centres or carrier traps that lead to the decrease of photocurrent in the patterned heterostructure. Photoluminescence decays of the heterostructure before and after patterning at 25 K are presented in figure 5.10. The decay time of the heterostructure decreases from 1 ns in the unpatterned structure to 250 ps in the patterned structure demonstrating the occurrence of surface states in the patterned structure. Consequently, photocurrent of the heterostructure decreases ~84% after the channel patterning, i.e. $I_{pattern} = 1\ \mu A$, $I_{flat} = 6.7\ \mu A$ at 570 nm excitation.

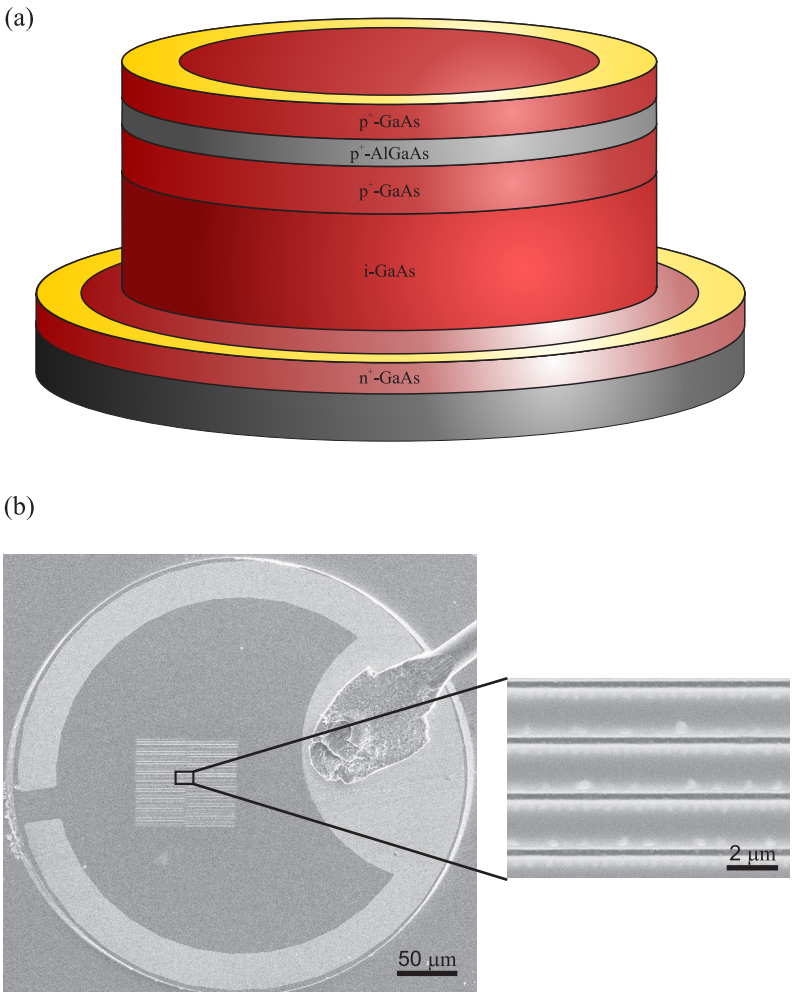

FIGURE 5.9: (a) Schematic diagram of the bulk heterostructure. (b) Scanning electron microscope (SEM) images of the patterned heterostructure. The inset shows the magnified image of the channels.

Since energy transfer rate (k_{ET}) is inversely proportional to the donor-acceptor separation distance, the resonant energy transfer rate decreases rapidly as the donor-acceptor separation distance increases. Therefore, carrier generation associated with resonant energy transfer takes place only within few nanometres from the top surface of the control device. Moreover, at 220 nm below the top surface there is a 43 nm thick layer of AlGaAs that hinders electrons generated in

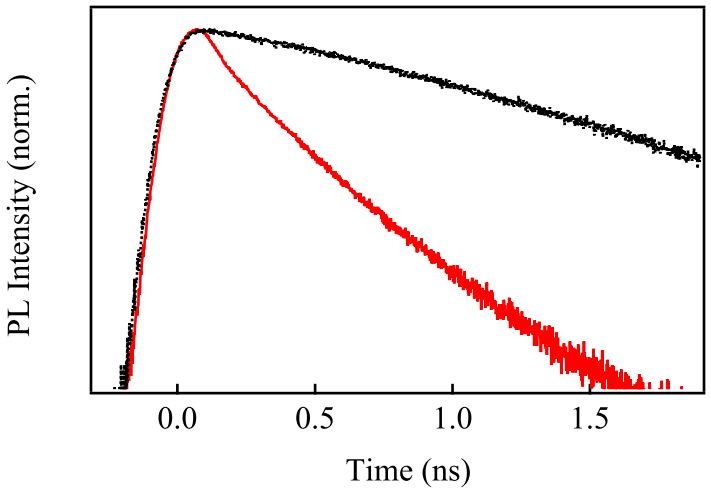

FIGURE 5.10: Photoluminescence decays of the flat (black solid line) and patterned (red solid line) heterostructures at 25 K.

the topmost layer to transport to the cathode. Hence, there should be no effect of resonant energy transfer on the photocurrent of the control structure. In contrast, owing to the channel structures, QDs are brought in close proximity to the active layer of the patterned heterostructure allowing for resonant energy transfer in the hybrid patterned device.

Another factor playing an important role in resonant energy transfer rate is the spectral overlap (Θ) between the donor emission and the acceptor absorption, i.e. k_{ET} scales linearly with Θ. Figure 5.11 shows the overlap between the QD emission and the photocurrent of the heterostructures where the emission peak of the QDs is around 758 nm at room temperature. Back energy transfer from the heterostructure to the QDs is inhibited considering the emission of the heterostructure and the absorption of the QDs. Furthermore, charge transport from CdTe QDs to GaAs heterostructures is prevented by the energy band offset of the QDs and the heterostructures.

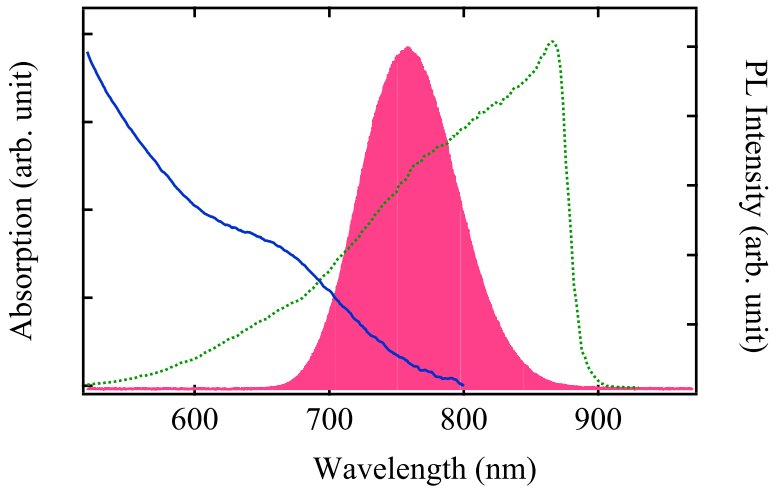

FIGURE 5.11: Spectral overlap of the hybrid structure at room temperature. The QD fluorescence is illustrated in pink and the QD absorption is plotted in the blue solid line. The green dotted line presents the photocurrent of the heterostructure.

To measure photocurrent of the hybrid structures, the hybrid structures are excited at 570 nm by an optical parametric amplifier (OPA) with 100 fs pulse width and a 250 kHz repetition rate. The excitation wavelength is chosen to minimise the effect of the direct excitation to photocurrent. The current-voltage characteristics of the bare patterned heterostructure and the hybrid patterned structure at 25 K and room temperature are shown in figure 5.12. Evidently, photocurrent of the hybrid patterned structure is higher than photocurrent of the bare patterned heterostructure. The higher photocurrent is attributed to resonant energy transfer in the hybrid patterned structure as discussed in the previous section. The advantage of the bulk heterostructure studied here over the QW heterostructure used in previous section is its higher carrier transport. In the case of the QW heterostructure, low energy carriers may be trapped in the QWs whereas the high energy carriers may experience phonon scattering resulting in the photocurrent reduction. In contrast, there is no such an obstruction in the bulk heterostructure. The QD emission energy is chosen in close proximity to the band edge of the bulk heterostructure in

order to decrease the possibility of phonon scattering. As a result, the photocurrent of the hybrid bulk heterostructure is about two orders of magnitude higher than that of the hybrid QW heterostructure.

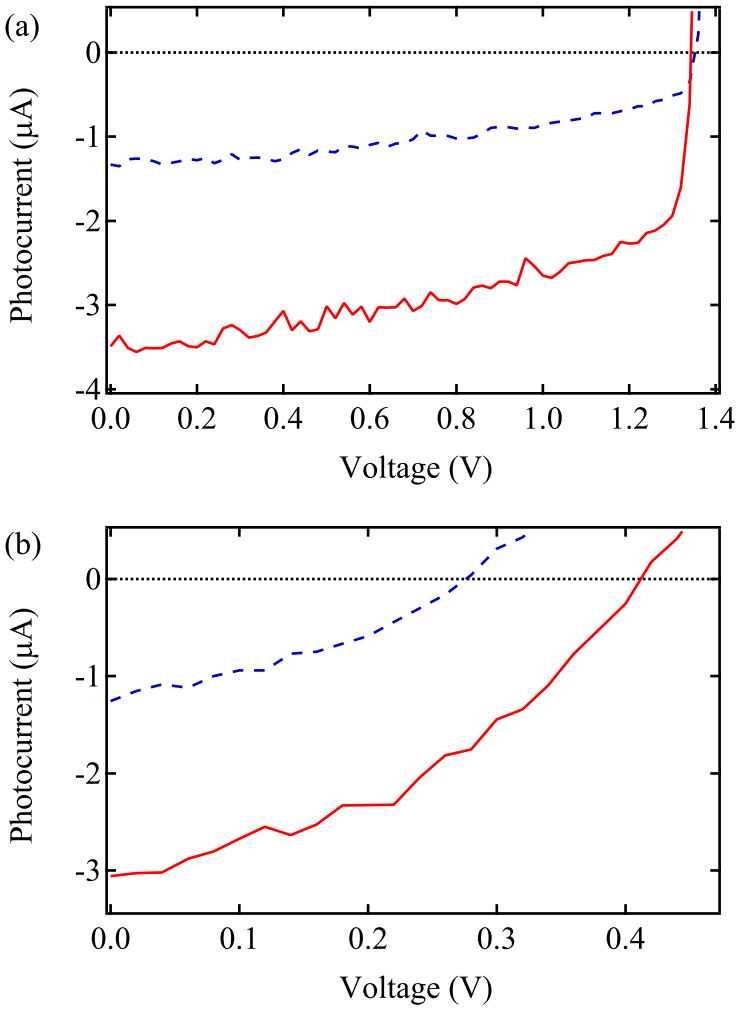

FIGURE 5.12: Current-voltage characteristics of the bare heterostructure (blue dashed line) and the hybrid patterned structure (red solid line) at (a) 25 K and (b) room temperature.

Photocurrent enhancement of the hybrid structure is given by $H = I_{hybrid}/I_{bare}$ where I_{hybrid} and I_{bare} are photocurrents of the hybrid and the bare structure respectively. From data in table 5.2, the photocurrent enhancement of the hybrid

patterned structure ($H_p = 3.00$) is higher than the enhancement of the hybrid flat structure ($H_f = 1.12$) at 25 K suggesting the occurrence of nonradiative energy transfer in the former. The slight increase of photocurrent in the hybrid flat structure is attributed to the conventional radiative energy transfer. Resonant energy transfer should have no effect on the photocurrent of the control device due to the large donor-acceptor separation distance. The photocurrent enhancement of the hybrid patterned slightly decreases at room temperature ($H_p = 2.44$) as a result of the reduced quantum yield of the QDs. Nevertheless, the photocurrent enhancement of the hybrid patterned structure still exceeds the enhancement of the hybrid control structure ($H_f = 1.07$). The corresponding monochromatic power conversion efficiency (η) of the hybrid device illuminated at 570 nm at 25 K and room temperature is determined from their current-voltage characteristics in figure 5.12 and shown in table 5.2. The power conversion efficiency is given by $\eta = \frac{I_m V_m}{P_i}$, where I_m and V_m are current and voltage that give maximum output power and P_i is input power from the light source. The enhancement of the power conversion efficiency provides further confirmation of the benefits offered by engineering nonradiative energy transfer in the hybrid device.

Although the photocurrent enhancement of the hybrid patterned structure is higher than that of the control structure, the photocurrent per excitation area of the former is lower than that of the latter. The surface states introduced to the heterostructures in the patterning process are crucial to the efficiency of the hybrid structures. In the hybrid QD/patterned QW structure discussed in the previous section, the CdSe/CdS QDs capped with hexadecylamine, tri-n-octylphosphine oxide, and tri-n-octylphosphine can passivate the surface states at the channel facets and a sixfold increase of photocurrent conversion efficiency is demonstrated. Here,

Sample description	25 K		RT	
	I (μA)	η (%)	I (μA)	η (%)
Bare patterned heterostructure	1.04	0.33	1.25	0.06
Hybrid QD/patterned heterostructure	3.14	1.13	3.05	0.26
Bare flat heterostructure	6.70	1.86	10.14	1.58
Hybrid QD/flat heterostructure	7.52	2.55	10.88	1.76

TABLE 5.2: Photocurrent and monochromatic power conversion efficiency at 570 nm excitation wavelength.

although the deposited QDs offer improved spectral overlap with the heterostructure, no passivation of the surface states is achieved exemplifying the specificity of the surface chemistry driven by the surface ligands and the solvent of the colloidal QDs.

There are several ways to improve the efficiency of the hybrid QD/patterned bulk heterostructures. For instance, the channel width and the size of the bars separated the channels can be optimised in order to increase the photocurrent. Photocurrent of the hybrid patterned structure can also be improved by engineering the top metal contact so that the photogenerated carriers can be collected more efficiently.

5.3.3 Summary

A hybrid colloidal QD/patterned bulk heterostructure is designed and fabricated to use in light harvesting applications. High absorption of colloidal QDs is utilised while their low carrier transfer efficiency is circumvented by using this configuration.

The advantage of the bulk heterostructure over the QW heterostructure used in the previous section is its higher carrier transport. The measured photocurrent increases significantly both at low temperature (25 K) and room temperature after depositing the QDs onto the bare patterned heterostructure and a threefold enhancement of photocurrent is observed demonstrating the potential of the proposed scheme in light harvesting applications.

Chapter 6

Conclusions

The integration of different types of materials into a hybrid structure provides a novel device possessing desirable properties of the individual constituent materials. Although materials such as organic polymers and colloidal QDs have excellent optical properties, they are known to have low carrier transfer efficiency. In contrast, semiconductor crystals have relatively high carrier mobility. By using the hybrid structure scheme, a device with superior optical and electrical properties can be achieved. Nevertheless, the efficient way to couple the constituent materials in a hybrid device remains challenging. Resonant energy transfer has been proposed to be an efficient mechanism to couple excitation states between materials of different classes such as the hybridisation of Frenkel excitons found in molecular materials and Wannier-Mott excitons found in semiconductor crystals. Hence, this thesis is focused on improving the performance of optoelectronic devices such as hybrid colour-conversion LEDs and hybrid PV cells by utilising resonant energy transfer.

A hybrid organic/inorganic semiconductor heterostructure where near-infrared cyanine dyes are deposited on the surface of a GaAs single QW is studied. The energy bands of the QW (donor) and the cyanine dyes (acceptors) are engineered so that the optical excitation energy of the QW can be transferred to the organic emitters via resonant energy transfer. The occurrence of resonant energy transfer in this hybrid structure is demonstrated at both donor and acceptor sites. The faster photoluminescence decay of the QW and the slower rise time of the cyanine dyes in the hybrid structure indicate an additional decay channel from the QW to the organic emitters.

In order to consider the hybrid structures as a practical lighting device, optical pumping should be replaced with electrical injection and high quality light in the visible region is required for rendering the true colour of objects. Hence, electrical injection is integrated into a hybrid structure consisting of colloidal QDs and a surface-patterned GaN-based LED. The emission of the hybrid structure can be simply chosen by changing the size or material compositions of the QD emitters. As a result of the close proximity of the donor and the acceptor in this surface-patterned configuration, the resonant energy transfer rate is improved. Consequently, a twofold enhancement of QD emission is demonstrated.

The second part of this thesis presents the studies of hybrid light harvesting devices. The concept of the hybrid device is to use a combination of colloidal QDs and semiconductor heterostructures where highly absorbing QDs and high carrier mobility heterostructures serve as photon absorbers and carrier transport media respectively. The emission energy of the QDs is tuned to the absorption spectrum of the heterostructures so that excitation energy of the QDs can be efficiently

transferred to the heterostructures via resonant energy transfer. After the transfer process, electron-hole pairs in the heterostructure are subsequently separated by the built-in electric field and collected by the corresponding electrodes.

To improve the resonant energy transfer rate, an array of rectangular channels is fabricated by a focused ion beam on the heterostructure surface penetrating through its active layers and subsequently filled with colloidal QDs. With this configuration, the QD donors are brought in close proximity to the active layers of the heterostructure. A sixfold enhancement of photocurrent conversion efficiency is demonstrated for the hybrid QD/patterned QW structure compared to a hybrid QD/flat QW structure suggesting the existence of resonant energy transfer in the former whereas the transfer process in the latter is only conventional radiative energy transfer. The existence of resonant energy transfer is evidently confirmed by time-resolved photoluminescence decays of the hybrid device.

Photocurrent of the hybrid structure is further improved by replacing the QW heterostructures with a bulk heterostructure. In the case of hybrid QW structure, carriers may be trapped by the QWs before collection by the electrodes: conversely, carrier transport is better for the bulk heterostructure. Moreover, the QD emission energy is tuned to the band edge of the bulk heterostructure in order to avoid nonradiative recombination of the energetic carriers in the heterostructure. Consequently, the photocurrent of the hybrid bulk heterostructure is about two orders of magnitude higher than that of the hybrid QW heterostructure.

List of publications

S. Chanyawadee, P. G. Lagoudakis, R. T. Harley, D. G. Lidzey, and M. Henini. Nonradiative exciton energy transfer in hybrid organic-inorganic heterostructures. Physical Review B, 77:193402, 2008.

S. Chanyawadee, R. T. Harley, M. Henini, D. V. Talapin, and P. G. Lagoudakis. Photocurrent enhancement in hybrid nanocrystal quantum-dot p-i-n photovoltaic devices. Physical Review Letters, 102:077402, 2009.

S. Chanyawadee, R. T. Harley, D. Taylor, M. Henini, A. S. Susha, A. L. Rogach and P. G. Lagoudakis. Efficient light harvesting in hybrid CdTe nanocrystal/bulk GaAs p-i-n photovoltaic devices. Applied Physics Letters, 94:233502, 2009.

S. Chanyawadee, P. G. Lagoudakis, R. T. Harley, D. Taylor, M. D. B. Charlton, D. V. Talapin and S. Lin. Increased color conversion efficiency in hybrid light emitting diodes utilizing nonradiative energy transfer. Advanced Materials.

List of conferences

S. Chanyawadee, S. Rohrmoser, J. Baldauf, S. Sapra, A. Eychmuller, I. M. Watson, M. Henini, D. Lidzey, R. T. Harley and P. G. Lagoudakis. Fluorescence energy transfer in hybrid semiconductor heterostructures: An alternative way of pumping fluorescent beads and organic emitters. MRS Fall Meeting, Boston (MA), USA, 2007.

S. Chanyawadee, R. T. Harley, M. Henini, P. G. Lagoudakis. Photocurrent enhancement in hybrid nanocrystal/patterned quantum well structure utilising nonradiative energy transfer. PLMCN8, Tokyo, Japan, 2008.

S. Chanyawadee, R. T. Harley, M. Henini and P. G. Lagoudakis. Multiplying photocurrent by utilising non-radiative energy transfer in hybrid nanocrystal/patterned quantum well structures. CLEO/QELS, San Jose (CA), USA, 2008.

S. Chanyawadee and P. G. Lagoudakis. Colloidal nanocrystals in hybrid semiconductor heterostructures for light harvesting and lighting applications. One Day Quantum Dot Meeting, Sheffield, UK, 2009.

Appendix A

Carrier Dynamics Modelling under Resonant Energy Transfer

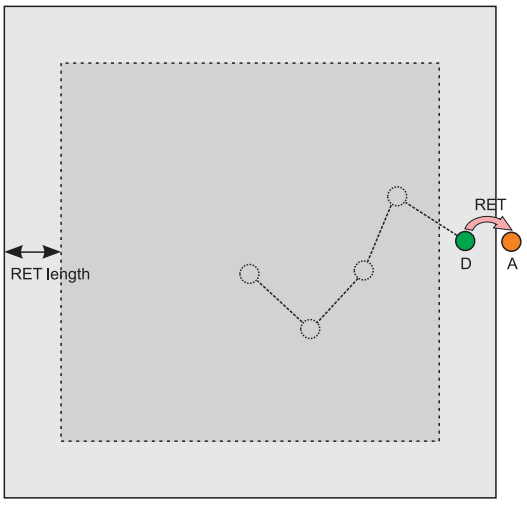

FIGURE A.1: Schematic diagram of the two-dimensional Monte Carlo simulation

A two-dimensional Monte Carlo simulation is established to investigate carrier dynamics under the effects of resonant energy transfer. The active layers of the deep etched LED shown in figure 4.2(a) is simplified to a two-dimensional layer with its dimensions corresponding to the perimeter percentage determined from the SEM image in figure 4.2(c). Carriers initially generated at random positions on the active layers move with thermal energy and randomly scatter with scattering centres. The direction of the carriers changes randomly after each scattering event. The resonant energy transfer length (RET length) is defined as the distance from the active layer/colloidal QD interface. Carriers at positions further than the RET length may recombine radiatively or nonradiatively following its intrinsic recombination rate whereas carriers at positions shorter than the RET length may additionally undergo resonant energy transfer. During the simulation, the number of carriers decaying either by intrinsic recombination or resonant energy transfer is recorded.

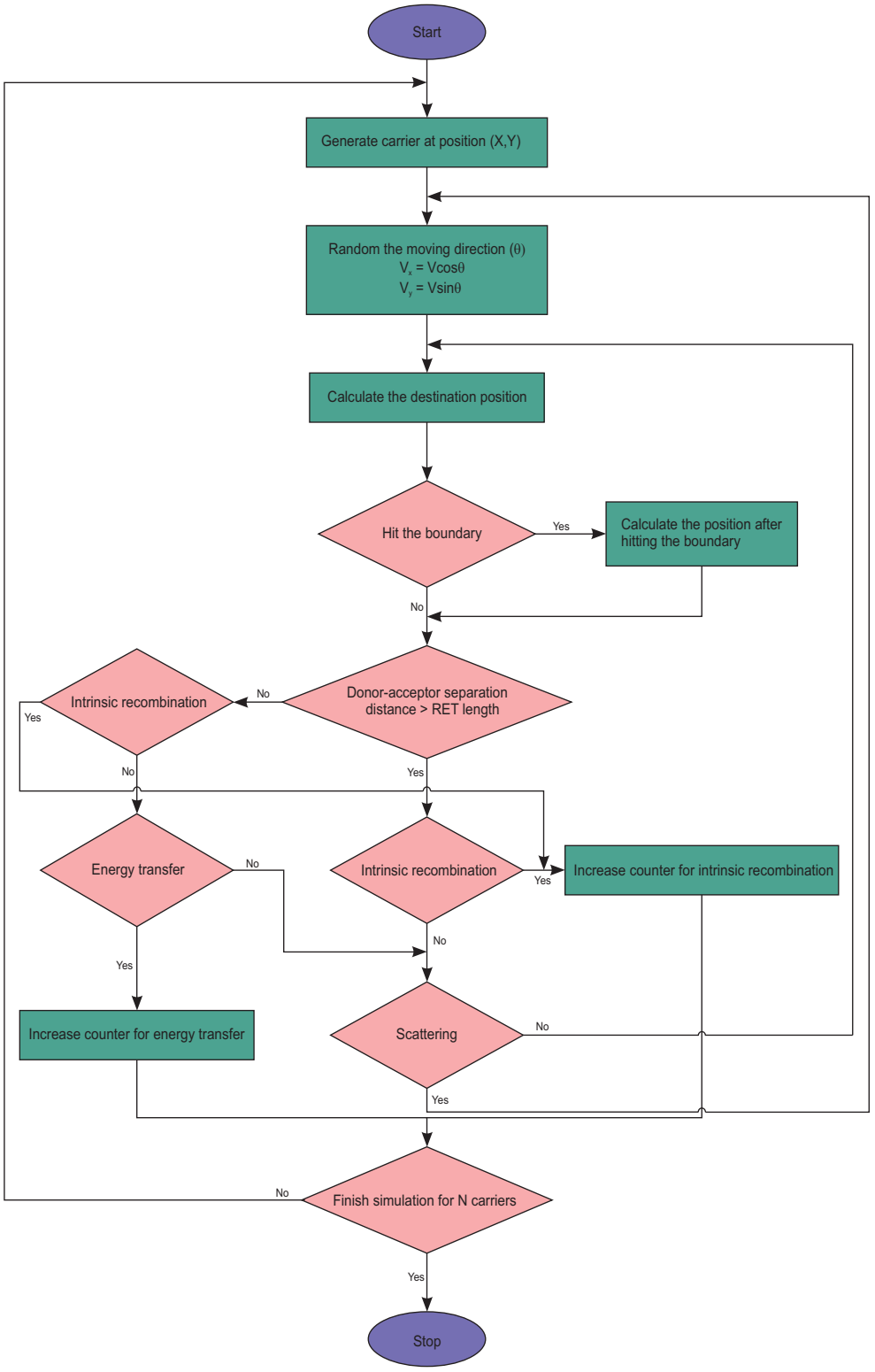

FIGURE A.2: Flow chart of the two-dimensional Monte Carlo simulation

Bibliography

[1] T. Förster. Zwischenmolekulare energiewanderung und fluorezenz. *Annalen der Physik*, 437:55, 1948.

[2] T Föster. Transfer mechanisms of electronic excitation. *Discussions of the Faraday Society*, 27:1–17, 1969.

[3] G. Cario and J. Franck. Über sensibilisierte fluoreszenz von gasen. *Zeitschrift für Physik A Hadrons and Nuclei*, 17:202–212, 1923.

[4] M. Achermann, M. A. Petruska, S. Kos, D. L. Smith, D. D. Koleske, and V. I. Klimov. Energy-transfer pumping of semiconductor nanocrystals using an epitaxial quantum well. *Nature*, 429:642–646, 2004.

[5] S. Lu and A. Madhukar. Nonradiative resonant excitation transfer from nanocrystal quantum dots to adjacent quantum channels. *Nano Letters*, 7: 3443–3451, 2007.

[6] S. Rohrmoser, J. Baldauf, R. T. Harley, P. G. Lagoudakis, S. Sapra, A. Eychmüller, and I. M. Watson. Temperature dependence of exciton transfer in hybrid quantum well/nanocrystal heterostructures. *Applied Physics Letters*, 91:092126, 2007.

[7] S. Blumstengel, S. Sadofev, C. Xu, J. Puls, and F. Henneberger. Converting Wannier into Frenkel excitons in an inorganic/organic hybrid semiconductor nanostructure. *Physical Review Letters*, 97:237401, 2006.

[8] S. Chanyawadee, P. G. Lagoudakis, R. T. Harley, D. G. Lidzey, and M. Henini. Nonradiative exciton energy transfer in hybrid organic-inorganic heterostructures. *Physical Review B*, 77:193402, 2008.

[9] J. Hill, S. Y. Heriot, O. Worsfold, T. H. Richardson, A. M. Fox, and D. D. C. Bradley. Controlled Förster energy transfer in emissive polymer Langmuir-Blodgett structures. *Physical Review B*, 69:041303, 2004.

[10] P. E. Shaw, A. Ruseckas, and I. D. W. Samuel. Distance dependence of excitation energy transfer between spacer-separated conjugated polymer films. *Physical Review B*, 78:245201, 2008.

[11] S. A. Crooker, J. A. Hollingsworth, S. Tretiak, and V. I. Klimov. Spectrally resolved dynamics of energy transfer in quantum-dot assemblies: Towards engineered energy flows in artificial materials. *Physical Review Letters*, 89: 186802, 2002.

[12] T. Franzl, T. A. Klar, S. Schietinger, A. L. Rogach, and J. Feldmann. Exciton recycling in graded gap nanocrystal structures. *Nano Letters*, 4:1599–1603, 2004.

[13] M. Achermann, M. A. Petruska, D. D. Koleske, M. H. Crawford, and V. I. Klimov. Nanocrystal-based light-emitting diodes utilizing high-efficiency nonradiative energy transfer for color conversion. *Nano Letters*, 6:1396–1400, 2006.

[14] M. Stockman. Light-emitting devices: From nano-optics to street lights. *Nature Materials*, 3:423–424, 2004.

[15] M. A. Baldo, D. F. O'Brien, Y. You, A. Shoustikov, S. Sibley, M. E. Thompson, and S. R. Forrest. Highly efficient phosphorescent emission from organic electroluminescent devices. *Nature*, 395:151–154, 1998.

[16] M. A. Baldo, M. E. Thompson, and S. R. Forrest. High-efficiency fluorescent organic light-emitting devices using a phosphorescent sensitizer. *Nature*, 403: 750–753, 2000.

[17] D. F. O'Brien, C. Giebeler, R. B. Fletcher, A. J. Cadby, L. C. Palilis, D. G. Lidzey, P. A. Lane, D. D. C. Bradley, and W. Blau. Electrophosphoresence from a doped polymer light emitting diode. *Synthetic Metals*, 116:379–383, 2001.

[18] M. Berggren, A. Dodabalapur, R. E. Slusher, and Z. Bao. Light amplification in organic thin films using cascade energy transfer. *Nature*, 389:466–469, 1997.

[19] G. Ramos-Ortiz, C. Spiegelberg, N. Peyghambarian, and B. Kippelen. Temperature dependence of the threshold for laser emission in polymer microlasers. *Applied Physics Letters*, 77:2783–2785, 2000.

[20] D. M. Willard and A. Van Orden. Quantum dots: Resonant energy-transfer sensor. *Nature Materials*, 2:575–576, 2003.

[21] C. Y. Zhang, H. C. Yeh, M. T. Kuroki, and T. H. Wang. Single-quantum-dot-based DNA nanosensor. *Nature Materials*, 4:826–831, 2005.

[22] S. Chanyawadee, R. T. Harley, M. Henini, D. V. Talapin, and P. G. Lagoudakis. Photocurrent enhancement in hybrid nanocrystal quantum-dot p-i-n photovoltaic devices. *Physical Review Letters*, 102:077402, 2009.

[23] K. Shankar, X. Feng, and C. A. Grimes. Enhanced harvesting of red photons in nanowire solar cells: Evidence of resonance energy transfer. *ACS Nano*, 3: 788–794, 2009.

[24] Toshio Nishida, Hisao Saito, and Naoki Kobayashi. Efficient and high-power AlGaN-based ultraviolet light-emitting diode grown on bulk GaN. *Applied Physics Letters*, 79:711–712, 2001.

[25] A. David, T. Fujii, R. Sharma, K. McGroddy, S. Nakamura, S. P. DenBaars, E. L. Hu, C. Weisbuch, and H. Benisty. Photonic-crystal GaN light-emitting diodes with tailored guided modes distribution. *Applied Physics Letters*, 88, 2006.

[26] I. Schnitzer, E. Yablonovitch, C. Caneau, T. J. Gmitter, and A. Scherer. 30% external quantum efficiency from surface textured, thin-film light-emitting diodes. *Applied Physics Letters*, 63:2174–2176, 1993.

[27] H. Kim, J. Cho, J. W. Lee, S. Yoon, H. Kim, C. Sone, Y. Park, and T. Y. Seong. Enhanced light extraction of GaN-based light-emitting diodes by using textured n-type GaN layers. *Applied Physics Letters*, 90:161110, 2007.

[28] H. G. Hong, S. S. Kim, D. Y. Kim, T. Lee, J. Song, J. H. Cho, C. Sone, Y. Park, and T. Y. Seong. Enhancement of the light output of GaN-based ultraviolet light-emitting diodes by a one-dimensional nanopatterning process. *Applied Physics Letters*, 88:103505, 2006.

[29] M. R. Krames, M. Ochiai-Holcomb, G. E. Hofler, C. Carter-Coman, E. I. Chen, I.-H. Tan, P. Grillot, N. F. Gardner, H. C. Chui, J.-W. Huang, S. A. Stockman, F. A. Kish, M. G. Craford, T. S. Tan, C. P. Kocot, M. Hueschen, J. Posselt, B. Loh, G. Sasser, and D. Collins. High-power truncated-inverted-pyramid $(Al_xGa_{1-x})_{0.5}In_{0.5}P$/GaP light-emitting diodes exhibiting $> 50\%$ external quantum efficiency. *Applied Physics Letters*, 75:2365–2367, 1999.

[30] J. J. Wierer, D. A. Steigerwald, M. R. Krames, J. J. O'Shea, M. J. Ludowise, G. Christenson, Y. C. Shen, C. Lowery, P. S. Martin, S. Subramanya, W. Gotz, N. F. Gardner, R. S. Kern, and S. A. Stockman. High-power AlGaInN flip-chip light-emitting diodes. *Applied Physics Letters*, 78:3379–3381, 2001.

[31] S. H. Fan, P. R. Villeneuve, J. D. Joannopoulos, and E. F. Schubert. High extraction efficiency of spontaneous emission from slabs of photonic crystals. *Physical Review Letters*, 78:3294–3297, 1997.

[32] A. A. Erchak, D. J. Ripin, S. Fan, P. Rakich, J. D. Joannopoulos, E. P. Ippen, G. S. Petrich, and L. A. Kolodziejski. Enhanced coupling to vertical radiation using a two-dimensional photonic crystal in a semiconductor light-emitting diode. *Applied Physics Letters*, 78:563–565, 2001.

[33] K. Kim, J. Choi, S. C. Jeon, J. S. Kim, and H. M. Lee. Photonic crystal effect on light emission from InGaN/GaN multi-quantum-well structures. *Applied Physics Letters*, 90:3, 2007.

[34] J. J. Wierer, A. David, and M. M. Megens. III-nitride photonic-crystal light-emitting diodes with high extraction efficiency. *Nature Photonics*, 3:163–169, 2009.

[35] K. S. Ramaiah, Y. K. Su, S. J. Chang, C. H. Chen, F. S. Juang, H. P. Liu, and I. G. Chen. Studies of InGaN/GaN multiquantum-well green-light-emitting diodes grown by metalorganic chemical vapor deposition. *Applied Physics Letters*, 85:401–403, 2004.

[36] N. S. Lewis. Toward cost-effective solar energy use. *Science*, 315:798–801, 2007.

[37] C. B. Murray, D. J. Norris, and M. G. Bawendi. Synthesis and characterization of nearly monodisperse CdE (E=S, Se, Te) semiconductor nanocrystallites. *Journal of the American Chemical Society*, 115:8706–8715, 1993.

[38] A. P. Alivisatos. Semiconductor clusters, nanocrystals, and quantum dots. *Science*, 271:933–937, 1996.

[39] J. Y. Kim, K. Lee, N. E. Coates, D. Moses, T. Q. Nguyen, M. Dante, and A. J. Heeger. Efficient tandem polymer solar cells fabricated by all-solution processing. *Science*, 317:222–225, 2007.

[40] M. J. Currie, J. K. Mapel, T. D. Heidel, S. Goffri, and M. A. Baldo. High-efficiency organic solar concentrators for photovoltaics. *Science*, 321:226–228, 2008.

[41] A. C. Arango, D. C. Oertel, Y. Xu, M. G. Bawendi, and V. Bulović. Heterojunction photovoltaics using printed colloidal quantum dots as a photosensitive layer. *Nano Letters*, 9:860863, 2009.

[42] A. J. Nozik. Quantum dot solar cells. *Physica E*, 14:115–120, 2002.

[43] S. A. McDonald, G. Konstantatos, S. G. Zhang, P. W. Cyr, E. J. D. Klem, L. Levina, and E. H. Sargent. Solution-processed PbS quantum dot infrared photodetectors and photovoltaics. *Nature Materials*, 4:138–142, 2005.

[44] C. Y. Liu, Z. C. Holman, and U. R. Kortshagen. Hybrid solar cells from P3HT and silicon nanocrystals. *Nano Letters*, 9:449–452, 2009.

[45] W. Shockley and H. J. Queisser. Detailed balance limit of efficiency of p-n junction solar cells. *Journal of Applied Physics*, 32:510–519, 1961.

[46] R. D. Schaller and V. I. Klimov. High efficiency carrier multiplication in PbSe nanocrystals: Implications for solar energy conversion. *Physical Review Letters*, 92:186601, 2004.

[47] D. G. Lidzey, D. D. C. Bradley, M. S. Skolnick, T. Virgili, S. Walker, and D. M. Whittaker. Strong exciton-photon coupling in an organic semiconductor microcavity. *Nature*, 395:53–55, 1998.

[48] D. G. Lidzey, D. D. C. Bradley, T. Virgili, A. Armitage, M. S. Skolnick, and S. Walker. Room temperature polariton emission from strongly coupled organic semiconductor microcavities. *Physical Review Letters*, 82:3316, 1999.

[49] E. Hanamura. Very large optical nonlinearity of semiconductor microcrystallites. *Physical Review B*, 37:1273, 1988.

[50] T. Takagahara. Biexciton states in semiconductor quantum dots and their nonlinear optical properties. *Physical Review B*, 39:10206, 1989.

[51] T. Kataoka, T. Tokizaki, and A. Nakamura. Mesoscopic enhancement of optical nonlinearity in CuCl quantum dots: Giant-oscillator-strength effect on confined excitons. *Physical Review B*, 48:2815, 1993.

[52] Y. Li, M. Takata, and A. Nakamura. Size-dependent enhancement of nonlinear optical susceptibilities due to confined excitons in CuBr nanocrystals. *Physical Review B*, 57:9193, 1998.

[53] M. A. Fox. *Optical properties of solids.* Oxford University Press Inc., New York, 2001.

[54] D. L. Dexter. A theory of sensitized luminescence in solids. *The Journal of Chemical Physics*, 21:836–850, 1953.

[55] I. Tanaka, Y. Tabata, and S. Tokito. Förster and Dexter energy-transfer processes in fluorescent BAlq thin films doped with phosphorescent $Ir(ppy)_3$ molecules. *Journal of Applied Physics*, 99:073501, 2006.

[56] S. R. Scully, P. B. Armstrong, C. Edder, J. M. J. Frechet, and M. D. McGehee. Long-range resonant energy transfer for enhanced exciton harvesting for organic solar cells. *Advanced Materials*, 19:2961–2966, 2007.

[57] X. F. Wang, Y. Koyama, Y. Wada, S. Sasaki, and H. Tamiaki. A dye-sensitized solar cell using pheophytin-carotenoid adduct: Enhancement of photocurrent by electron and singlet-energy transfer and by suppression of singlet-triplet annihilation due to the presence of the carotenoid moiety. *Chemical Physics Letters*, 439:115–120, 2007.

[58] M. J. Walter, N. J. Borys, K. J. van Schooten, and J. M. Lupton. Light-harvesting action spectroscopy of single conjugated polymer nanowires. *Nano Letters*, 8:3330–3335, 2008.

[59] D. Timmerman, I. Izeddin, P. Stallinga, I. N. Yassievich, and T. Gregorkiewicz. Space-separated quantum cutting with silicon nanocrystals for photovoltaic applications. *Nature Photonics*, 2:105–109, 2008.

[60] G. Heliotis, P. N. Stavrinou, D. D. C. Bradley, E. Gu, C. Griffin, C. W. Jeon, and M. D. Dawson. Spectral conversion of ingan ultraviolet microarray light-emitting diodes using fluorene-based red-, green-, blue-, and white-light-emitting polymer overlayer films. *Applied Physics Letters*, 87, 2005.

[61] S. Nizamoglu, E. Sari, J. H. Baek, I. H. Lee, and H. V. Demir. White light generation by resonant nonradiative energy transfer from epitaxial InGaN/-GaN quantum wells to colloidal CdSe/ZnS core/shell quantum dots. *New Journal of Physics*, 10:123001, 2008.

[62] A. Camposeo, F. D. Benedetto, R. Cingolani, and D. Pisignano. Full color control and white emission from conjugated polymer nanofibers. *Applied Physics Letters*, 94:043109, 2009.

[63] J. Lee, A. O. Govorov, and N. A. Kotov. Bioconjugated superstructures of CdTe nanowires and nanoparticles: Multistep cascade Förster resonance energy transfer and energy channeling. *Nano Letters*, 5:2063–2069, 2005.

[64] G. D. Scholes. Long-range resonance energy transfer in molecular systems. *Annual Review of Physical Chemistry*, 54:57–87, 2003.

[65] V. M. Agranovich, D. M. Basko, G. C. La Rocca, and F. Bassani. Excitons and optical nonlinearities in hybrid organic-inorganic nanostructures. *Journal of Physics: Condensed Matter*, 10:9369–9400, 1998.

[66] G. Heliotis, G. Itskos, R. Murray, M. D. Dawson, I. M. Watson, and D. D. C. Bradley. Hybrid inorganic/organic semiconductor heterostructures with efficient non-radiative energy transfer. *Advanced Materials*, 18:334–338, 2006.

[67] S. Kos, M. Achermann, V. I. Klimov, and D. L. Smith. Different regimes of Förster-type energy transfer between an epitaxial quantum well and a proximal monolayer of semiconductor nanocrystals. *Physical Review B*, 71:205309, 2005.

[68] A. R. Clapp, I. L. Medintz, J. M. Mauro, B. R. Fisher, M. G. Bawendi, and H. Mattoussi. Fluorescence resonance energy transfer between quantum dot donors and dye-labeled protein acceptors. *Journal of the American Chemical Society*, 126:301–310, 2004.

[69] V. L. Colvin, M. C. Schlamp, and A. P. Alivisatos. Light-emitting-diodes made from cadmium selenide nanocrystals and a semiconducting polymer. *Nature*, 370:354–357, 1994.

[70] M. Segal, M. Singh, K. Rivoire, S. Difley, T. Van Voorhis, and M. A. Baldo. Extrafluorescent electroluminescence in organic light-emitting devices. *Nature Materials*, 6:374–378, 2007.

[71] Q. Sun, Y. A. Wang, L. S. Li, D. Y. Wang, T. Zhu, J. Xu, C. H. Yang, and Y. F. Li. Bright, multicoloured light-emitting diodes based on quantum dots. *Nature Photonics*, 1:717–722, 2007.

[72] J. M. Caruge, J. E. Halpert, V. Wood, V. Bulovic, and M. G. Bawendi. Colloidal quantum-dot light-emitting diodes with metal-oxide charge transport layers. *Nature Photonics*, 2:247–250, 2008.

[73] Cree Press Release, (Cree, Inc., Durham, UK, 19 November 2008); http://www.cree.com/press/press_detail.asp?i=1227101620851.

[74] V. Cleave, G. Yahioglu, P. Le Barny, R. H. Friend, and N. Tessler. Harvesting singlet and triplet energy in polymer LEDs. *Advanced Materials*, 11:285–288, 1999.

[75] R. H. Friend, R. W. Gymer, A. B. Holmes, J. H. Burroughes, R. N. Marks, C. Taliani, D. D. C. Bradley, D. A. Dos Santos, J. L. Bredas, M. Logdlund, and W. R. Salaneck. Electroluminescence in conjugated polymers. *Nature*, 397:121–128, 1999.

[76] S. Coe, W. K. Woo, M. Bawendi, and V. Bulović. Electroluminescence from single monolayers of nanocrystals in molecular organic devices. *Nature*, 420: 800–803, 2002.

[77] C. D. Muller, A. Falcou, N. Reckefuss, M. Rojahn, V. Wiederhirn, P. Rudati, H. Frohne, O. Nuyken, H. Becker, and K. Meerholz. Multi-colour organic light-emitting displays by solution processing. *Nature*, 421:829–833, 2003.

[78] Universal Display Corporation Press Release, (Universal Display Corporation, New Jersy, USA, 17 June, 2008); http://www.universaldisplay.com/downloads/Press%20Releases/2008/PANL_whitemilestone_FINAL.pdf.

[79] Sony Press Release, (Sony Corporation, Tokyo, Japan, 1 October 2007); http://www.sony.net/SonyInfo/News/Press/200710/07-1001E/index.html.

[80] F. So, J. Kido, and P. Burrows. Organic light-emitting devices for solid-state lighting. *MRS Bulletin*, 33:663–669, 2008.

[81] P. S. Davids, S. M. Kogan, I. D. Parker, and D. L. Smith. Charge injection in organic light-emitting diodes: Tunneling into low mobility materials. *Applied Physics Letters*, 69:2270–2272, 1996.

[82] G. D. Sharma, V. S. Choudhary, and M. S. Roy. Electrical and photovoltaic properties of devices based on PbPc-TiO_2 thin films. *Solar Energy Materials and Solar Cells*, 91:1087–1096, 2007.

[83] G. E. Jabbour, J.-F. Wang, and N. Peyghambarian. High-efficiency organic electrophophorescent devices through balance of charge injection. *Applied Physics Letters*, 80:2026–2028, 2002.

[84] G. L. Ma, G. Z. Ran, A. G. Xu, Y. H. Xu, Y. P. Qiao, W. X. Chen, L. Dai, and G. G. Qin. Improving charge-injection balance and cathode transmittance of top-emitting organic light-emitting device with p-type silicon anode. *Applied Physics Letters*, 87:081106, 2005.

[85] A. Shah, P. Torres, R. Tscharner, N. Wyrsch, and H. Keppner. Photovoltaic technology: The case for thin-film solar cells. *Science*, 285:692–698, 1999.

[86] R. R. King, D. C. Law, K. M. Edmondson, C. M. Fetzer, G. S. Kinsey, H. Yoon, R. A. Sherif, and N. H. Karam. 40% efficient metamorphic GaInP/ GaInAs/Ge multijunction solar cells. *Applied Physics Letters*, 90, 2007.

[87] M. Gratzel. Photoelectrochemical cells. *Nature*, 414:338–344, 2001.

[88] W. U. Huynh, J. J. Dittmer, and A. P. Alivisatos. Hybrid nanorod-polymer solar cells. *Science*, 295:2425–2427, 2002.

[89] I. Gur, N. A. Fromer, M. L. Geier, and A. P. Alivisatos. Air-stable all-inorganic nanocrystal solar cells processed from solution. *Science*, 310:462–465, 2005.

[90] W. U. Huynh, X. G. Peng, and A. P. Alivisatos. CdSe nanocrystal rods/poly(3-hexylthiophene) composite photovoltaic devices. *Advanced Materials*, 11:923–927, 1999.

[91] I. Gur, N. A. Fromer, C. P. Chen, A. G. Kanaras, and A. P. Alivisatos. Hybrid solar cells with prescribed nanoscale morphologies based on hyperbranched semiconductor nanocrystals. *Nano Letters*, 7(2):409–414, 2007.

[92] V. Agranovich, H. Benisty, and C. Weisbuch. Organic and inorganic quantum wells in a microcavity: Frenkel-Wannier-Mott excitons hybridization and energy transformation. *Solid State Communications*, 102:631–636, 1997.

[93] J. Wenus, R. Parashkov, S. Ceccarelli, A. Brehier, J. S. Lauret, M. S. Skolnick, E. Deleporte, and D. G. Lidzey. Hybrid organic-inorganic exciton-polaritons in a strongly coupled microcavity. *Physical Review B*, 74, 2006.

[94] R. J. Holmes, S. Kena-Cohen, V. M. Menon, and S. R. Forrest. Strong coupling and hybridization of Frenkel and Wannier-Mott excitons in an organic-inorganic optical microcavity. *Physical Review B*, 74, 2006.

[95] J. Wenus, S. Ceccarelli, D. G. Lidzey, A. I. Tolmachev, J. L. Slominskii, and J. L. Bricks. Optical strong coupling in microcavities containing J-aggregates absorbing in near-infrared spectral range. *Organic Electronics*, 8:120–126, 2007.

[96] H. Kuhn. Classical aspects of energy transfer in molecular systems. *The Journal of Chemical Physics*, 53:101–108, 1970.

[97] G. Itskos, G. Heliotis, P. G. Lagoudakis, J. Lupton, N. P. Barradas, E. Alves, S. Pereira, I. M. Watson, M. D. Dawson, J. Feldmann, R. Murray, and D. D. C. Bradley. Efficient dipole-dipole coupling of Mott-Wannier and Frenkel excitons in (Ga,In)N quantum well/polyfluorene semiconductor heterostructures. *Physical Review B*, 76:035344, 2007.

[98] D. V. Talapin, R. Koeppe, S. Gotzinger, A. Kornowski, J. M. Lupton, A. L. Rogach, O. Benson, J. Feldmann, and H. Weller. Highly emissive colloidal CdSe/CdS heterostructures of mixed dimensionality. *Nano Letters*, 3:1677–1681, 2003.

[99] P. O. Anikeeva, C. F. Madigan, J. E. Halpert, M. G. Bawendi, and V. Bulovic. Electronic and excitonic processes in light-emitting devices based on organic materials and colloidal quantum dots. *Physical Review B*, 78:085434, 2008.

[100] D. Basko, G. C. La Rocca, F. Bassani, and V. M. Agranovich. Förster energy transfer from a semiconductor quantum well to an organic material overlayer. *The European Physical Journal B*, 8:353–362, 1999.

[101] T. Wang, H. Saeki, J. Bai, T. Shirahama, M. Lachab, S. Sakai, and P. Eliseev. Effect of silicon doping on the optical and transport properties of InGaN/-GaN multiple-quantum-well structures. *Applied Physics Letters*, 76:1737–1739, 2000.

[102] C. A. Chang, C. F. Shih, N. C. Chen, T. Y. Lin, and K. S. Liu. In-rich $In_{1-x}Ga_xN$ films by metalorganic vapor phase epitaxy. *Applied Physics Letters*, 85:6131–6133, 2004.

[103] X. Brokmann, L. Coolen, M. Dahan, and J. P. Hermier. Measurement of the radiative and nonradiative decay rates of single cdse nanocrystals through a controlled modification of their spontaneous emission. *Physical Review Letters*, 93:107403, 2004.

[104] D. S. Chemla, D. A. B. Miller, P. W. Smith, A. C. Gossard, and W. Wiegmann. Room-temperature excitonic nonlinear absorption and refraction in GaAs/AlGaAs multiple quantum well structures. *IEEE Journal of Quantum Electronics*, 20:265–275, 1984.

[105] T. Sizer, T. K. Woodward, U. Keller, K. Sauer, T. H. Chiu, D. L. Sivco, and A. Y. Cho. Measurement of carrier escape rates, exciton saturation intensity, and saturation density in electrically biased multiple-quantum-well modulators. *IEEE Journal of Quantum Electronics*, 30:399–407, 1994.

[106] A. L. Rogach, T. Franzl, T. A. Klar, J. Feldmann, N. Gaponik, V. Lesnyak, A. Shavel, A. Eychmüller, Y. P. Rakovich, and J. F. Donegan. Aqueous synthesis of thiol-capped CdTe nanocrystals: State-of-the-art. *Journal of Physical Chemistry C*, 111:14628–14637, 2007.